Article

Cell cycle duration determines oncogenic transformation capacity

https://doi.org/10.1038/s41586-025-08935-x

Received: 26 August 2023

Accepted: 25 March 2025

Published online: 30 April 2025

Open access

Check for updates

Danian Chen[1,2,3,4], Suying Lu[1], Katherine Huang[1], Joel D. Pearson[1,15], Marek Pacal[1], Phillipos Peidis[1], Sean McCurdy[1], Tao Yu[1], Monika Sangwan[1], Angela Nguyen[1], Philippe P. Monnier[2,5], Daniel Schramek[1,6], Liang Zhu[7,8,9,16], David Santamaria[10], Mariano Barbacid[11], Nagako Akeno[12], Kathryn A. Wikenheiser-Brokamp[13,14] & Rod Bremner[1,2,3]✉

Oncogenic mutations are widespread in normal human tissues[1]. Similarly, in murine chimeras, cells carrying an oncogenic lesion contribute normal cells to adult tissues without causing cancer[2–4]. How lineages that escape cancer via normal development differ from the minority that succumb is unclear. Tumours exhibit characteristic cancer hallmarks; we therefore searched for hallmarks that differentiate cancer-prone lineages from resistant lineages. Here we show that total cell cycle duration (T_c) predicts transformation susceptibility across multiple tumour types. Cancer-prone *Rb*- and *p107*-deficient retina (*Rb* is also known as *Rb1* and *p107* is also known as *Rbl1*) exhibited defects in apoptosis, senescence, immune surveillance, angiogenesis, DNA repair, polarity and proliferation. Perturbing the SKP2–p27–CDK2/CDK1 axis could block cancer without affecting these hallmarks. Thus, cancer requires more than the presence of its hallmarks. Notably, every tumour-suppressive mutation that we tested increased T_c, and the T_c of the cell of origin of retinoblastoma cells was half that of resistant lineages. T_c also differentiated the cell of origin in $Rb^{-/-}$ pituitary cancer. In lung, loss of *Rb* and *p53* (also known as *Trp53*) transforms neuroendocrine cells, whereas $Kras^{G12D}$ or $Braf^{V600E}$ mutations transform alveolar type 2 cells[5–7]. The shortest T_c consistently identified the cell of origin, regardless of mutation timing. Thus, relative T_c is a hallmark of initiation that distinguishes cancer-prone from cancer-resistant lineages in several settings, explaining how mutated cells escape transformation without inducing apoptosis, senescence or immune surveillance.

Cancers are initiated with distinct genetic alterations, which indicates that they constitute context-specific responses. Loss of *Ptch1* or *Ctnnb* (also known as *Ctnnb1*) triggers medulloblastoma from distinct cells of origin, and activated *Kras* mutations induce ectopic division in many lung epithelial cell types but transforms primarily alveolar type 2 (AT2) pneumocytes[7,8]. The reason for lineage-specific cancer susceptibility is usually obscure. Cell death can underlie cancer resistance[9], but humans carry millions of normal cells with oncogenic mutations[1], indicating that there is an 'escape mechanism' whereby most of these cells do not develop into tumours. The *Rb* tumour suppressor gene is a well known example. Systemic *Rb* loss causes extensive, cell-autonomous ectopic mitoses in multiple mouse embryonic tissues[10,11]. In chimeras generated by injecting $Rb^{-/-}$ embryonic stem (ES) cells into wild-type blastocysts, mutant cells contribute half of nearly all adult tissues, yet all organs except the pituitary remain tumour-free[2,3]. Thus, normal development—and not cell death, senescence or immune clearance—is the escape mechanism for trillions of $Rb^{-/-}$ cells. Similarly, ectopic division—but not cancer—is common in tissue-specific *Rb*-knockout mice, and removing the *Rb* relatives *p107* and *p130* (also known as *Rbl2*) increases tumorigenesis, but most cell types remain resistant[12–14]. Indeed, cancer-free cell survival with normal development is the typical response to oncogenic insults (for example, in refs. 4,7). Insight into this mechanism of cancer resistance could reveal new preventative and therapeutic strategies.

Established tumours share cancer hallmarks[15]. We sought to uncover a hallmark that distinguishes cancer-prone and cancer-resistant lineages that survive oncogenic events. Starting with retinoblastoma,

[1]Lunenfeld–Tanenbaum Research Institute, Mount Sinai Hospital, Sinai Health System, Toronto, Ontario, Canada. [2]Department of Ophthalmology and Visual Science, University of Toronto, Toronto, Ontario, Canada. [3]Department of Laboratory Medicine and Pathobiology, University of Toronto, Toronto, Ontario, Canada. [4]Department of Ophthalmology, Research Laboratory of Ophthalmology and Vision Sciences, Eye Research Institute, West China Hospital, Sichuan University, Chengdu, China. [5]Donald K. Johnson Eye Institute, Krembil Research Institute, University Health Network, Department of Physiology, Faculty of Medicine, University of Toronto, Toronto, Ontario, Canada. [6]Department of Molecular Genetics, University of Toronto, Toronto, Ontario, Canada. [7]Department of Developmental and Molecular Biology, The Albert Einstein Comprehensive Cancer Center and Liver Research Center, Albert Einstein College of Medicine, Bronx, NY, USA. [8]Department of Ophthalmology and Visual Sciences, The Albert Einstein Comprehensive Cancer Center and Liver Research Center, Albert Einstein College of Medicine, Bronx, NY, USA. [9]Department of Medicine, The Albert Einstein Comprehensive Cancer Center and Liver Research Center, Albert Einstein College of Medicine, Bronx, NY, USA. [10]Molecular Mechanisms of Cancer Program, Centro de Investigación del Cáncer, Consejo Superior de Investigaciones Científicas (CSIC)–University of Salamanca, Salamanca, Spain. [11]Molecular Oncology Program, National Center for Cancer Research (CNIO), Madrid, Spain. [12]Division of Pathology and Laboratory Medicine, Cincinnati Children's Hospital Medical Center, Cincinnati, OH, USA. [13]The Perinatal Institute Division of Pulmonary Biology, Cincinnati Children's Hospital Medical Center, Cincinnati, OH, USA. [14]Department of Pathology and Laboratory Medicine, University of Cincinnati College of Medicine, Cincinnati, OH, USA. [15]Present address: CancerCare Manitoba Research Institute and Department of Pharmacology and Therapeutics, University of Manitoba, Winnipeg, Manitoba, Canada. [16]Deceased: Liang Zhu. ✉e-mail: bremner@lunenfeld.ca

we blocked tumorigenesis and assessed effects on cancer hallmarks, reasoning that features that are always altered by tumour suppression might also predict cancer susceptibility. One hallmark, total cell cycle duration (T_c), fulfilled these criteria.

Strategies to block retinoblastoma

The mouse retina, similar to most human tissues, resists transformation upon *Rb* loss. Co-deleting *Rb*-related genes can cause cancer, but this only occurs in specific lineages[16–18]. In the *Rb*$^{-/-}$;*p107*$^{-/-}$ retina, all seven differentiating cell types divide ectopically, and whereas four undergo apoptosis, three survive[16]. Horizontal and Müller cells eventually exit the cell cycle, resisting cancer, whereas tumours arise from the amacrine lineage[16]. Tumours become evident microscopically at postnatal day 8 (P8)[16], and are visible macroscopically after around 100 days (Fig. 1a).

Consistent with RB controlling multiple cancer hallmarks (https://cancer.sanger.ac.uk/cosmic/census-page/RB) the *Rb*$^{-/-}$;*p107*$^{-/-}$ retina exhibits ectopic division, cell-specific apoptosis resistance, altered differentiation, DNA damage, disrupted polarity, aberrant angiogenesis and absence of senescence or immune surveillance[16,17,19–21]. We searched for interventions that suppress tumorigenesis, and then for altered hallmarks that always accompany tumour suppression. We then investigated whether such hallmarks distinguish the cancer-prone lineage from cancer-resistant lineages. We focused first on SKP2, part of the SKP1–cullin–F-box complex (SCF^{SKP2}) that ubiquitylates cyclin-dependent kinase (CDK) inhibitors such as p27 (encoded by *Cdkn1b*, also known as *p27*), targeting them for degradation, as the SKP2–p27–CDK axis is linked to *Rb*$^{-/-}$ cancer[22,23]. As shown below, we observed unexpected differences in the effect of *Skp2* homozygosity or heterozygosity on cancer hallmarks. We thus further interrogated this axis by manipulating p27 or CDKs. SKP2, p27 and CDKs regulate proliferation and many other processes. Thus, SKP2-mediated ubiquitylation regulates DNA repair, autophagy, apoptosis, adhesion and epithelial-to-mesenchyme transition, and E3 ligase-independent SKP2 functions affect genes associated with transcription, apoptosis and migration[24]. p27, independently of CDKs, regulates stemness, migration and microtubules[25]. CDK2 and CDK1 regulate differentiation and epigenetics[26,27] and CDK1 also regulates apoptosis, Golgi, nuclear–cytosolic transport and vesicle transport[28]. Given this broad repertoire, we expected that tumour suppression would alter multiple cancer hallmarks.

To assess SKP2, we crossed *α-cre;Rb*$^{f/f}$;*p107*$^{-/-}$;*Skp2*$^{+/-}$ mice. The *α-cre* transgene targets the embryonic peripheral retina, and 45% (37 out of 78) of eyes of *α-cre;Rb*$^{f/f}$;*p107*$^{-/-}$ (hereafter referred to as DKO) mice developed tumours[16] (Fig. 1a). Deleting two (DKO-*Skp2*$^{-/-}$, 0 out of 44 eyes developed tumours) or one (DKO-*Skp2*$^{+/-}$, 0 out of 40 eyes developed tumours) *Skp2* allele blocked tumorigenesis (Fig. 1a). Heterozygosity reduced the amount of SKP2 protein by nearly twofold (Extended Data Fig. 1a) and increased the amount of p27 protein in total lysate by around 1.4-fold; immunofluorescence revealed an 18-fold increase in the fraction of p27^{+} amacrine cells, the cell of origin of the tumours (5.4% in DKO mice versus 90% in DKO-*Skp2*$^{+/-}$ mice) (Extended Data Fig. 1b–d).

To assess p27, we utilized two knock-in alleles. The product of the *p27*$^{CK-}$ allele cannot bind CDK2–cyclin, and DKO-*Skp2*$^{+/-}$;*p27*$^{CK-/CK-}$ tissue developed retinoblastoma quickly (Fig. 1b). Thus, preventing p27 binding to CDK2–cyclin binding overrides the protective effect of *Skp2* heterozygosity. *p27*^{T187A} (hereafter *p27*^{KI}) prevents recognition of SCF^{SKP2}. We observed some increase in total p27 in DKO-*p27*$^{KI/+}$ or DKO-*p27*$^{KI/KI}$ contexts, similar to that seen in DKO-*Skp2*$^{+/-}$ retina but less than in DKO-*Skp2*$^{-/-}$ retina (Extended Data Fig. 1b), but *p27*^{KI} increased the number of p27-positive amacrine cells (Extended Data Fig. 1c,d). One copy blocked retinoblastoma development (0 out of 40 eyes developed tumours), phenocopying *Skp2* heterozygosity (Fig. 1a,b). Thus, SKP2 inactivation of p27 is critical for retinoblastoma development.

CDK2 activity correlates with retinoblastoma susceptibility[23]. We also assessed CDK1, as it compensates for CDK2 (refs. 29–31). We targeted both *Cdk2* alleles and/or one allele of *Cdk1*, which is essential for cell division[32]. *Cdk2* deletion reduced tumorigenesis, although to a lower extent than *Skp2* heterozygosity, suggesting partial redundancy, and although *Cdk1* heterozygosity had no effect, tumorigenesis was almost completely suppressed in *Cdk1*$^{+/-}$;*Cdk2*$^{-/-}$ retinas (Fig. 1c).

Apoptosis, senescence or immunity

Leveraging these six tumour-suppressing manipulations (*Skp2*$^{-/-}$, *Skp2*$^{+/-}$, *p27*$^{KI/+}$, *p27*$^{KI/KI}$, *Cdk2*$^{-/-}$ and *Cdk2*$^{-/-}$;*Cdk1*$^{+/-}$) we searched for consistently affected cancer hallmarks. Tumours in the DKO model emerge microscopically at around P8—many cancer hallmarks are evident at this stage, and whereas cancer-prone amacrine and cancer-resistant horizontal and Müller cells all undergo ectopic division during this window, the cancer-resistant horizontal and Müller cells gradually stop dividing such that by around P30 only tumours derived from amacrine cells continue to proliferate[16]. Thus, we focused on P4–P21 to assess how tumour suppression affects cancer hallmarks.

First, we assessed whether tumour suppression increased cell death, senescence or immune infiltration (Fig. 1d–i and Extended Data Fig. 1e–i). In DKO retina, all differentiating lineages divide ectopically, and amacrine, horizontal and Müller cells resist apoptosis, whereas the other lineages undergo E2F-driven apoptosis[19,33]. *p107*$^{-/-}$ mice served as controls[16]. Ectopic division thickens the DKO retina by P8 and P10, but apoptosis of the four death-prone cell types reduces its thickness by P21 (ref. 16) (Extended Data Fig. 1e). At P8, P10 and P21, the DKO-*Skp2*$^{-/-}$ retina was much thinner, yet surprisingly, cancer-resistant DKO-*Skp2*$^{+/-}$ retina did not differ from cancer-prone DKO retina at any time point (Extended Data Fig. 1e).

Skp2 loss can promote *Rb*$^{-/-}$ cell apoptosis[22]; increased death might therefore explain why *Skp2* deletion suppresses retinoblastoma. Horizontal cells (marked by ONECUT2 expression) did not vary between control, DKO, DKO-*Skp2*$^{+/-}$ and DKO-*Skp2*$^{-/-}$ retinas at P10 or P21, and Müller glia (marked by SOX9) were increased in DKO versus control retinas and further increased with heterozygous or homozygous *Skp2* loss (Fig. 1d). Heterozygous or homozygous *Skp2* loss reduced the number of amacrine cells (marked by AP2A) in the DKO versus control retinas (Fig. 1d), but immunostaining or western blot of active cleaved caspase-3 revealed that, DKO, DKO-*Skp2*$^{+/-}$ and DKO-*Skp2*$^{-/-}$ retinas exhibited similar proportions of dying cells at P4, P8, P10 or P21, which were even reduced in P8 and P10 DKO-*Skp2*$^{-/-}$ retina (Fig. 1e and Extended Data Fig. 1g). The percentage of AP2A^{+} cleaved caspase-3-positive cells among all AP2A^{+} amacrine cells was also invariant between DKO, DKO-*Skp2*$^{+/-}$ and DKO-*Skp2*$^{-/-}$ retinas at P4 or P8 (Fig. 1f). Similarly, total or amacrine cell apoptosis was not increased in the DKO-*p27*$^{KI/+}$, DKO-*p27*$^{KI/KI}$, DKO-*Cdk2*$^{-/-}$ or DKO-*Cdk2*$^{-/-}$;*Cdk1*$^{+/-}$ retinas (Fig. 1e,f and Extended Data Fig. 1g). Thus, increased cell death does not explain the tumour-suppressive effect of manipulating the SKP2–p27–CDK axis.

Skp2 loss can drive senescence[34], but at P4 and P8, all genotypes exhibited only background senescence-associated β-galactosidase staining, and whereas the DKO-*Skp2*$^{-/-}$ or DKO-*p27*$^{KI/KI}$ retina became senescent by P10, with senescence persisting at P21 and beyond, other genotypes that suppress tumorigenesis (*Skp2*$^{+/-}$, *p27*^{KI}, *Cdk2*$^{-/-}$ and *Cdk2*$^{-/-}$;*Cdk1*$^{+/-}$) did not induce senescence (Fig. 1g and Extended Data Fig. 1h).

Next, we assessed immune infiltrate. Fluorescence-activated cell sorting (FACS) of dissociated tumour-prone DKO and tumour-resistant DKO-*Skp2*$^{+/-}$ retina revealed negligible levels of B cells, T cells, natural killer (NK) cells, macrophages/microglia and leukocytes (Fig. 1h). Quantification of galectin 3 (GAL3)-expressing microglia also revealed no inflammatory response in tumour-prone retina, which was unchanged in the six genotypes that suppressed tumorigenesis (Fig. 1i and Extended Data Fig. 1i). Thus, tumour suppression could occur independently of increased death, senescence or immune infiltration (Extended Data Fig. 2).

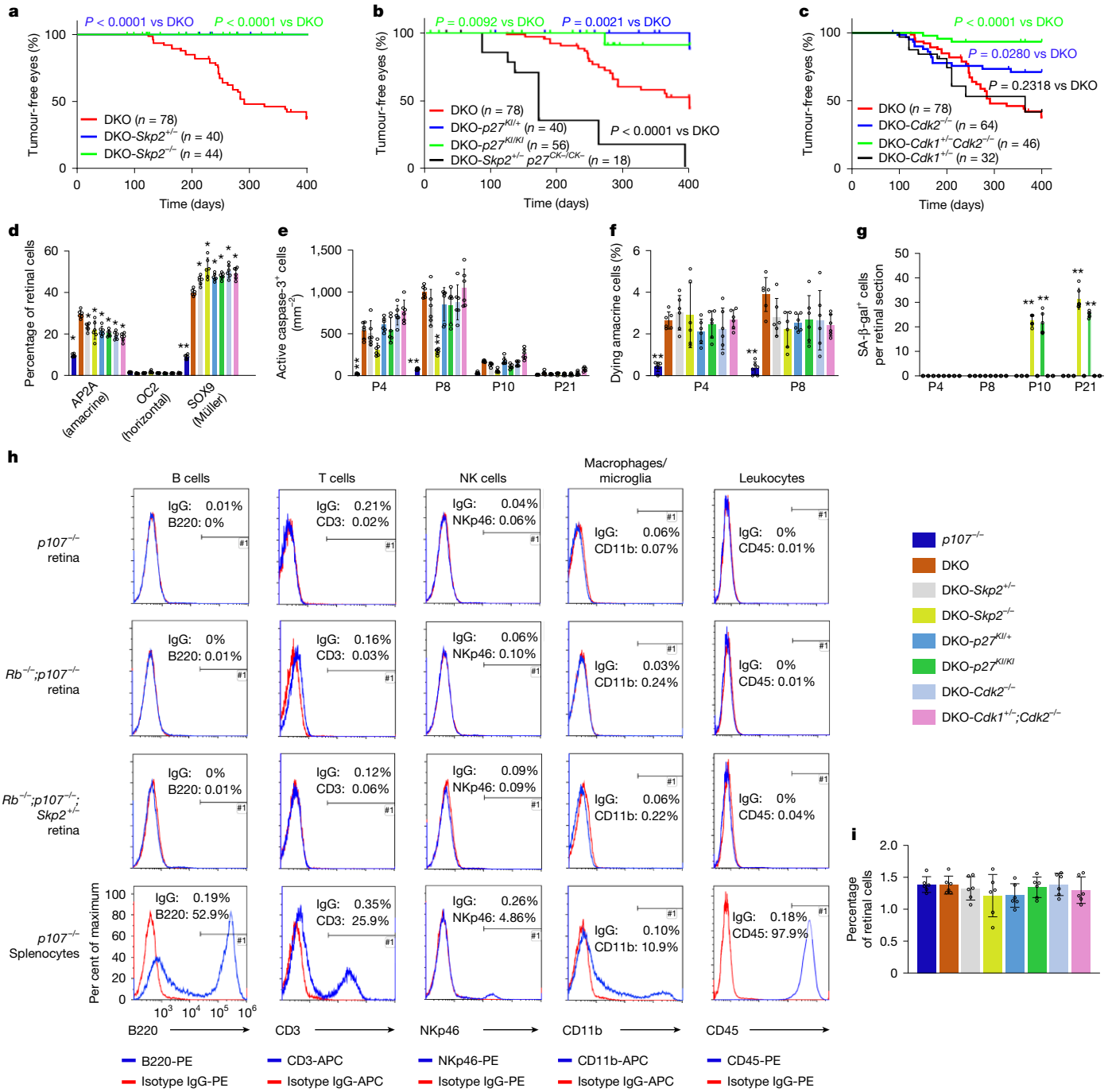

Fig. 1 | Tumour suppression without increasing cell death, senescence or immune infiltration. a–**c**, Kaplan–Meier curves showing how *Skp2*$^{+/-}$ and *Skp2*$^{-/-}$ (**a**), *p27*$^{KI/+}$, *p27*$^{KI/KI}$ and *Skp2*$^{+/-}$;*p27*$^{CK-/CK-}$ (**b**) and *Cdk2*$^{-/-}$ and *Cdk1*$^{+/-}$;*Cdk2*$^{-/-}$ (**c**) genotypes affect tumorigenesis in the DKO mouse retina. *P* values by log-rank (Mantel–Cox) test comparing indicated genotypes with DKO. **d**, Quantification of AP2A^{+} (amacrine), ONECUT2-expressing (OC2^{+}) (horizontal) and SOX9^{+} (Müller) cells in P10 retina of indicated mouse genotypes as a percentage of all retinal cells. **e**, Active caspase-3^{+} cells in retinas of indicated ages and genotypes. **f**, Percentage of AP2A^{+} active caspase-3^{+} cells among all AP2A^{+} amacrine cells. **g**, Counts of senescence-associated β-galactosidase-expressing (SA-β-gal^{+}) cells per retinal section. **h**, Representative flow cytometry histograms showing the proportion of B220^{+} B cells, CD3^{+} T cells, NKp46^{+} natural killer (NK) cells, CD11b^{+} macrophage/microglial cells and CD45^{+} leukocytes in P8 retina and spleen. **i**, Quantification of GAL3^{+} microglia of P8 retina as a percentage of all retinal cells. Data in **d**–**g**,**i** are mean ± s.d. ($n = 6$ mice per cohort), and asterisks indicate a significant difference between indicated genotypes and DKO; one-way analysis of variance (ANOVA) with Bonferroni correction. *$P < 0.05$; **$P < 0.01$.

DNA repair, angiogenesis or polarity

SKP2 can promote DNA repair[35], but the proportion of γH2AX^{+} cells was unaltered in *Skp2*$^{-/-}$ and *Skp2*$^{+/-}$ retina (Fig. 2a,b). Similarly, *p27*^{KI}, *p27*$^{KI/KI}$, *Cdk2*$^{-/-}$ or *Cdk2*$^{-/-}$;*Cdk1*$^{+/-}$ mutations did not ameliorate DNA damage (Fig. 2a,b). Tumour suppression also did not alter DNA damage in the cell of origin (Supplementary Fig. 2).

In postnatal retina, blood vessels invade from the tissue surface around P7 to form intra-retinal vessels, but because *Rb* loss kills O_2-requiring neurons, the *Rb*$^{-/-}$ retina lacks intra-retinal (deep vascular

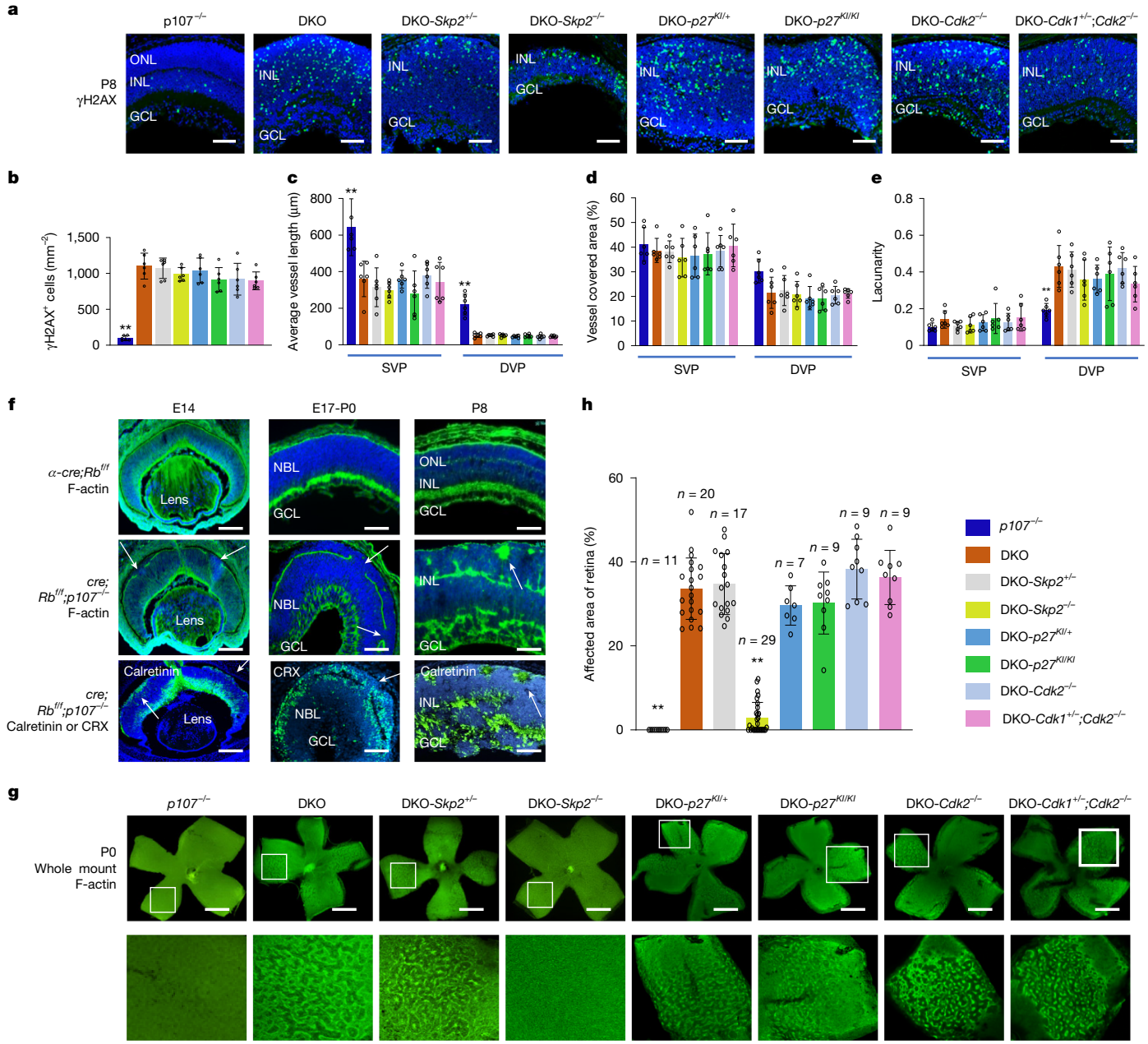

Fig. 2 | Tumour suppression without altering DNA damage, aberrant angiogenesis or apical polarity defects. a, Horizontal retinal sections of retina from P8 mice of indicated genotypes were stained for nuclei (DAPI, blue) and DNA damage (γH2AX, green). GCL, ganglion cell layer; INL, inner nuclear layer; ONL, outer nuclear layer. Scale bars, 50 μm. **b**, Quantification of γH2AX$^+$ cell density in retina from **a**. **c**–**e**, Quantification of mean vessel length (**c**), vessel coverage area (**d**) and lacunarity (**e**) of isolectin B4 (IB4)-stained whole-mount P8 retinas of indicated genotypes. SVP, superficial vascular plexus. **f**, Horizontal retinal sections from mice of the indicated ages and genotypes were stained for DAPI (blue) and markers that detect F-actin at adherens junctions (green), amacrine cells (calretinin, green) and photoreceptor precursors (CRX, green). Arrows indicate breaks in the outer limiting membrane at E14 or E17-P0, or rosettes at P8. NBL, neuroblast layer. Scale bars, 50 μm. **g**, Whole-mount retinas of P0 mice of the indicated genotypes were stained for F-actin (green). Scale bars, 200 μm. **h**, Area of disrupted F-actin staining in **g** as a percentage of the whole retina. Experiments were repeated independently with similar results at least three times in **a**,**f** and two times in **g** for each mouse. Data are mean ± s.d. (n = 6 mice (**b**–**e**) and 9–29 mice (**h**) per group as indicated). Asterisks indicate significant difference compared with DKO by one-way ANOVA with Bonferroni correction.

plexus (DVP)) vessels, whereas superficial vascular plexus remains unaffected[20]. The DVP is also absent in *Rb*$^{-/-}$;*p107*$^{-/-}$ retina[21] (Extended Data Fig. 3a,b). None of the six cancer-suppressing manipulations resulted in improved DVP (Fig. 2c–e and Extended Data Fig. 3a, b).

Apical polarity is disrupted in the DKO retina[36]. In embryonic retina, each apical cell membrane has a ring of adherens junctions linked by filamentous actin (F-actin). In cross-sections, they appear as a continuous line (the outer limiting membrane) that separates apical and basolateral domains. This outer limiting membrane was intact in cancer-resistant *Rb*$^{-/-}$ retina but disrupted in cancer-prone *Rb*$^{-/-}$;*p107*$^{-/-}$ retina (Fig. 2f). A second inverted retina formed at the back of the eye, with CRX$^+$ photoreceptors on the inner surface and calretinin$^+$ (encoded by *Calb2*) amacrine cells on the outer surface (Fig. 2f). By P8 the dual retinas fused and resolved into amacrine rosettes (Fig. 2f). In DKO whole mounts, abnormal F-actin staining was apparent in the peripheral α-Cre-expressing retina; we therefore quantified the abnormal tissue area (Extended Data Fig. 3c). We used *p107*$^{-/-}$ retina as a control (Fig. 2g), as it retained the polarity seen in wild-type or *Rb*$^{-/-}$ retina

(Extended Data Fig. 3d). The polarity defects seen in the DKO retina were almost completely rescued in DKO-*Skp2*$^{-/-}$ retina (Fig. 2g,h)—this was supported by cross-sections stained for atypical PKCλ/ι and N-cadherin (Extended Data Fig. 3d). By contrast, none of the other five tumour-suppressing genotypes that we tested rescued polarity defects (Fig. 2g,h and Extended Data Fig. 3d). *Skp2*$^{-/-}$ may rescue polarity by inhibiting CDK to levels below that obtained with p27^{KI}, and indeed *Skp2* loss induced more p27 than p27^{KI} (Extended Data Fig. 1b). Nonetheless, the results show that RB and p107 maintain, whereas SKP2 disrupts, apical polarity. More importantly, multiple genetic manipulations suppress tumorigenesis without correcting apical polarity (Extended Data Fig. 2). Notably, our data demonstrate that cancer-prone and cancer-resistant tissue can exhibit the same set of cancer hallmarks. Thus, a cancer initiation hallmark must exist that is more sensitive to *Skp–p27–Cdk* mutations than survival, senescence, immune infiltration, DNA repair, angiogenesis or apical polarity.

Tumour suppression without lineage change

The proportion of AP2A^{+} amacrine cells was reduced, without increased cell death, in tumour-resistant genotypes (Fig. 1d–f), implicating altered differentiation or division. We used multiple approaches to assess these hallmarks. First, using single-cell RNA sequencing (scRNA-seq) we compared P8 tumour-prone DKO retina with cancer-free DKO-*Skp2*$^{+/-}$ retina. Tumour growth begins around this time, progenitors (usually the only dividing cells) are almost depleted, their death-prone differentiating descendants are either gone (ganglion cells) or depleted (bipolar cells and photoreceptors), and there is extensive ectopic division among surviving amacrine and Müller cells, and horizontal cells make up only around 0.2% of wild-type retina and less than 4% of the tumour-prone retina[16]. We obtained scRNA-seq data for 3,621 DKO cells with 52,983 mapped reads per cell and 2,200 genes per cell, and 5,196 DKO-*Skp*$^{+/-}$ cells with 31,520 reads per cell and 1,873 genes per cell. Genotype did not affect rare astrocytes or immune cells (Extended Data Fig. 4a), confirming prior analyses (Fig. 1h,i and Extended Data Fig. 1i). Initial analysis using uniform manifold approximation and projection (UMAP) generated clusters biased by cell cycle phase, which we regressed out to focus on lineage, generating 13 clusters (Extended Data Fig. 4b–f), which were consolidated (Extended Data Fig. 4g–i and Supplementary Table 1) into 7 annotated clusters (Fig. 3a). Top differentially expressed genes (DEGs) included known markers such as *Apoe* (marker for Müller glia (Mu cluster)), *Rom1* (photoreceptors (PR)), *Ebf1* (amacrine precursors (AmP)), *Pcsk1n* (mature amacrine cells (AmM)), *Fbxo5* (rare remaining mitotic progenitors (ProgM)), *Isl1* (bipolar cells (BiP)) and *Otx2*, *Neurod1* and *Neurod4* (neurogenic (Neu)) (Fig. 3b, Extended Data Fig. 4g, Supplementary Table 2 and Methods). Genotype barely affected BiP, Mu, Neu, PR and ProgM clusters but, matching AP2A staining (Fig. 1d), tumour-free DKO-*Skp2*$^{+/-}$ retina had 1.7× fewer AmM cells and 1.4× fewer AmP cells (Fig. 3c). Seurat cell cycle phase classification revealed that tumour suppression reduced the number of AmP cluster cells in S and G2/M phase twofold, with smaller effects in other clusters (Fig. 3d). Differential expression analysis revealed induction of cell cycle genes in tumour-prone AmP and, to a lesser extent, Mu and Neu clusters (Fig. 3e and Supplementary Tables 3 and 4). Hypergeometric analysis revealed enrichment of *Cdk2* (ref. 37) as well as G2/M and S phase signature genes in DKO AmP, Mu and Neu clusters (Fig. 3e,f and Supplementary Tables 3 and 5). These data implicate cell cycle rather than lineage in tumour suppression.

To further examine whether *Skp2*$^{+/-}$ affects *Rb*$^{-/-}$;*p107*$^{-/-}$ cell lineage we performed retroviral clonal analyses. We interbred *Rb*$^{f/f}$;*p107*$^{-/-}$;*Skp2*$^{+/-}$ mice, injected P0 pups subretinally with low-titre Cre–GFP retrovirus to knockout *Rb* and mark progenitors, and then scored cell types in GFP^{+} clones at P21. P0 progenitors generate rods, Müller glia, and bipolar and amacrine cells. The proportion of clones with at least one of these cell types would change if there was a lineage effect, but the proportion of DKO and DKO-*Skp2*$^{+/-}$ clones with these cell types were identical (Fig. 3g). Thus, scRNA-seq and clonal analyses indicate that *Skp2* heterozygosity does not alter lineage.

T_c marks the retinal cell of origin

To further interrogate the cell cycle, we assessed Ki67 index at P4, P8, P10 and P21. This marker for dividing cells disappears within a day in newborn post-mitotic differentiating retinal neurons[38], but remains in ectopically dividing differentiating *Rb*$^{-/-}$ cells[16,23]. Most DKO cells gradually stop dividing within 1–2 months of birth[16]. *Skp2* status had no effect at P4, P8 or P10, whereas at P21 the Ki67 index was 19% in DKO retina but negligible in DKO-*Skp2*$^{-/-}$ tissue (Fig. 4a). However, *Skp2*$^{+/-}$, *p27*^{KI}, *p27*$^{KI/KI}$, *Cdk2*$^{-/-}$ or *Cdk2*$^{-/-}$;*Cdk1*$^{+/-}$ mutations did not affect proliferation index at any time (Fig. 4a). We also assessed proliferation index with ten different markers (Extended Data Fig. 5a) that label various clusters (Extended Data Fig. 5b,c). Relative to DKO, *Skp2* loss affected two out of the ten populations, but the other five tumour-suppressive genotypes had no effect (Extended Data Fig. 5a). Thus, perturbations of the SKP2–p27–CDK axis can prevent cancer initiation without altering the proportion of dividing cells.

Proliferation index does not reflect cell cycle duration, and a 30-min pulse of 5-bromo-2′-deoxyuridine (BrdU) at P8 revealed that tumour-suppressing mutations reduce the proportion of cells in S phase (Fig. 4b). Fewer S phase cells could reflect increased duration of other phases or shortening of S phase, increasing or decreasing the duration of the cell cycle duration, respectively. To quantify T_c or S phase duration (T_s), we used staggered 5-ethynyl-2′-deoxyuridine (EdU)–BrdU double labelling[39]. P8 mice were first pulsed with EdU and then with BrdU 2.5 h later, and sections were stained for these markers plus Ki67 to calculate T_c and T_s (Supplementary Figs. 3 and 4a). The six tumour-suppressing genotypes had little effect on T_s, but increased average T_c in the DKO tissue from 41 h to 62 h (*Skp2*$^{+/-}$), 107 h (*Skp2*$^{-/-}$), 69 h (*p27*$^{KI/+}$), 81 h (*p27*$^{KI/KI}$), 53 h (*Cdk2*$^{-/-}$) or 60 h (*Cdk2*$^{-/-}$;*Cdk1*$^{+/-}$) (Fig. 4c).

As all tumour-suppressing mutations increased the duration of the cell cycle, we explored whether the cell of origin had a distinct T_c. We applied quadruple labelling using EdU, BrdU, Ki67 and cell-type markers to compare T_c and T_s in cancer-prone AP2A^{+} amacrine cells versus cancer-resistant SOX9^{+} Müller or ONECUT2^{+} horizontal cells (Supplementary Figs. 3c and 4b–d). Notably, T_c of DKO amacrine cells was only 26 h, compared with 143 h for Müller cells and 77 h for horizontal cells, whereas T_s was similar for all cell types (Fig. 4d). Thus, the cell of origin divides faster than cancer-resistant cell types. Moreover, T_c of *Skp2*$^{-/-}$, *Skp2*$^{+/-}$, *p27*$^{KI/+}$, *p27*$^{KI/KI}$, *Cdk2*$^{-/-}$ and *Cdk2*$^{-/-}$;*Cdk1*$^{+/-}$ DKO amacrine cells was 109 h, 43 h, 41 h, 46 h, 33 h and 39 h, respectively, compared with 26 h for DKO amacrine cells (Fig. 4d). Notably, the reduced effect of CDK loss parallels its weaker tumour-suppressive effects (Fig. 1c). We further measured cell cycle duration in AmP cells expressing PTF1A, which drives the amacrine lineage upstream of AP2A[40]. T_c in DKO PTF1A^{+} cells was 28.3 h, compared with 44.4 h, 60.9 h, 44.2 h, 44.2 h, 41.1 h and 42.4 h in *Skp2*$^{+/-}$, *Skp2*$^{-/-}$, *p27*$^{KI/+}$, *p27*$^{KI/KI}$, *Cdk2*$^{-/-}$, and *Cdk2*$^{-/-}$;*Cdk1*$^{+/-}$ DKO PTF1A^{+} cells, respectively, and only *Skp2*$^{-/-}$ affected T_s (Extended Data Fig. 5d). Other populations, such as those expressing p21 or MYCN that primarily mark Neu cells, did not show a consistent increase in T_c with tumour-suppressing mutations (Extended Data Fig. 5b,d). Thus, tumour suppression always affects T_c of the cell of origin, and the cell of origin has the shortest T_c (Extended Data Fig. 2).

T_c as a general initiation hallmark

Relative T_c may only distinguish the cell of origin for retinoblastoma. To assess the generality of this effect, we surveyed additional cancer models. In *Rb*$^{+/-}$ pituitary, 100% of mice develop *Rb*$^{-/-}$ intermediate lobe cancer but only around 20% develop anterior lobe tumours[41].

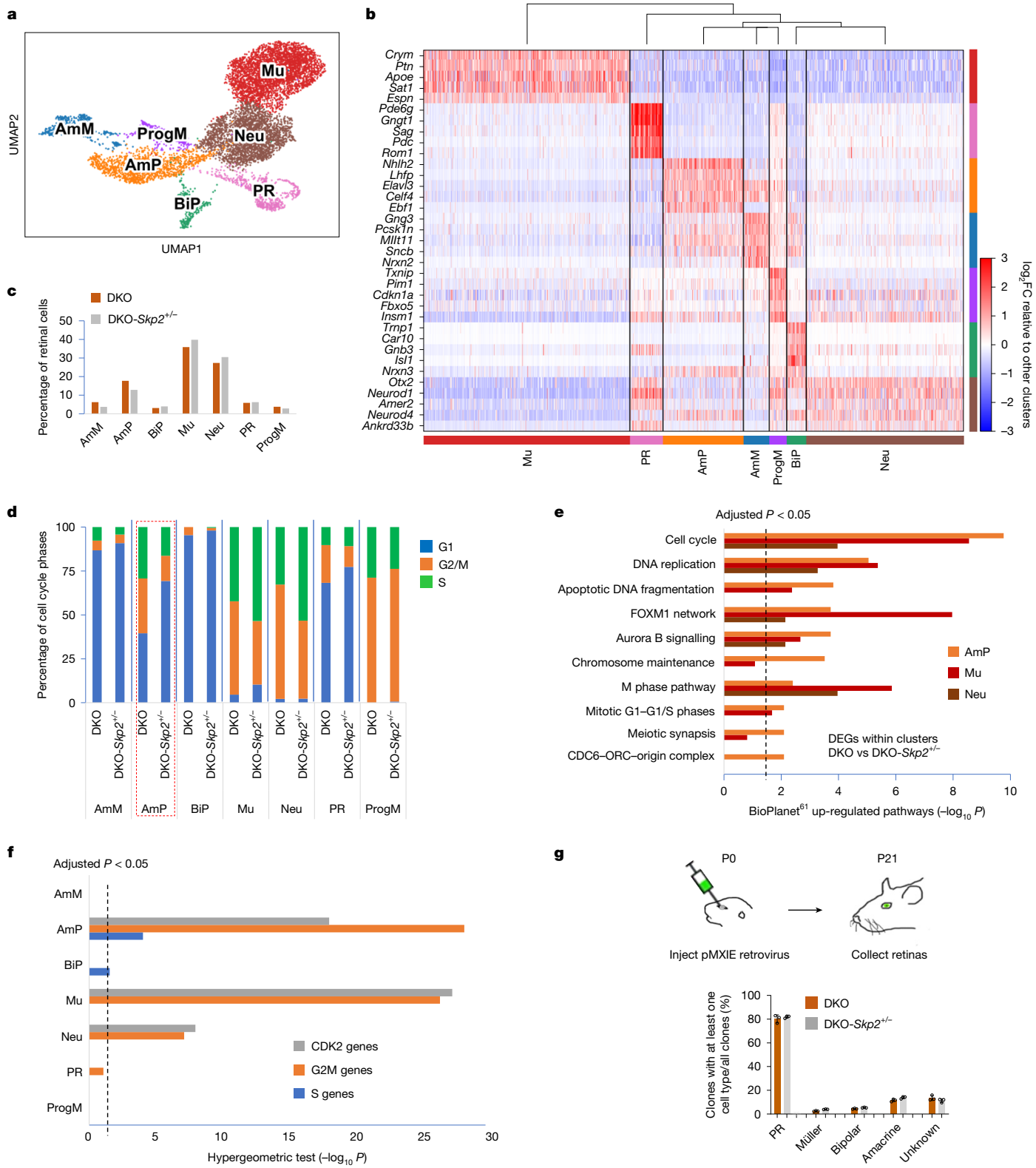

Fig. 3 | Tumour suppression without altering cell lineage. a, UMAP analysis of scRNA-seq data from P8 DKO and DKO-*Skp2*$^{+/-}$ retinas. **b**, Heat map of top five DEGs. Dendrogram shows the relatedness of the seven clusters. $\log_2$FC, $\log_2$ fold change. **c**, Proportion of cells in each cluster. **d**, Seurat analysis of the proportions of cells in each phase of the cell cycle. The red outline highlights the AmP cluster. **e**, Enriched gene lists in DKO versus DKO-*Skp2*$^{+/-}$ AmP, Mu and Neu clusters. BioPlanet[61] available at https://tripod.nih.gov/bioplanet/. **f**, Enrichment of cell cycle gene signatures among genes that are up-regulated in DKO retina. **g**, P0 *Rb*$^{f/f}$;*p107*$^{-/-}$;*Skp2*$^{+/-}$ pups received subretinal injection of low-titre Cre–GFP retrovirus to knockout *Rb*, and cell types in GFP$^+$ clones were scored at P21. Data are mean ± s.d. (n = 3 mice per group).

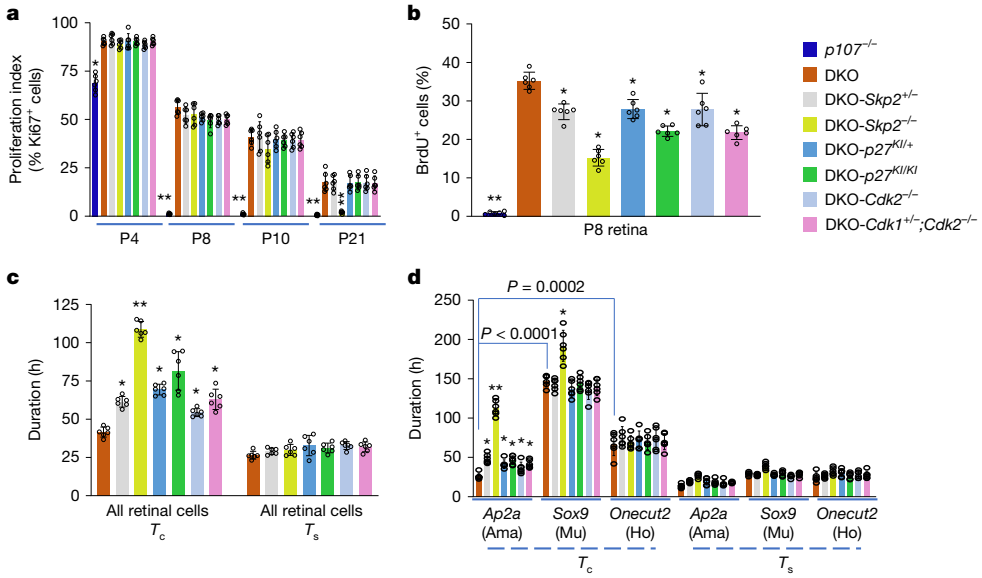

Fig. 4 | Tumour suppression extends T_c, and the cell of origin has the shortest T_c. a, Proliferation index in retina from mice of the indicated genotypes and ages. **b**, Percentage of BrdU$^+$ cells in P8 retinas of the indicated genotypes. **c**, Total cell cycle (T_c) and S phase (T_s) duration of all dividing (Ki67$^+$) cells in retina of the indicated genotypes at P8. **d**, T_c and T_s in amacrine (Ama), Müller (Mu) or horizontal (Ho) cells in retina of the indicated genotypes at P8. Data are mean ± s.d. ($n = 6$ mice per cohort as indicated by bars). Asterisks indicate significant difference compared with DKO by one-way ANOVA with Bonferroni correction. Exact *P* values are indicated for comparisons with amacrine (AP2A$^+$) and Müller (SOX9$^+$) or horizontal (ONECUT2$^+$) cells in DKO retinas by two-tailed unpaired *t*-test.

To assess T_c, we injected *creERT2;LSL-tdTomato;Rb$^{f/f}$* mice with tamoxifen at four or eight weeks of age, then two weeks later applied staggered EdU–BrdU labelling and assessed tissue at six and ten weeks of age. *LSL-tdTomato;Rb$^{f/f}$* mice served as wild-type controls. Nearly all intermediate lobe and anterior lobe *creERT2;LSL-tdTomato;Rb$^{f/f}$* cells were positive for tdTomato, and all mice developed intermediate lobe cancer despite ectopic division in both intermediate lobe and anterior lobe (Supplementary Fig. 5a,b). Proliferation index was higher for intermediate lobe than anterior lobe cells at ten weeks but similar in six-week-old mice (Extended Data Fig. 6a); thus, proliferation index does not reliably predict cancer susceptibility. Pro-opiomelacortin (POMC), which is expressed in all intermediate lobe cells and around 20% of anterior lobe cells, is cleaved to generate adrenocorticotropic hormone in the anterior lobe and melanocyte stimulating hormone (MSHα) in the intermediate lobe. MSHα antibodies label both these POMC lineages, which are easily distinguished by intermediate lobe versus anterior lobe locations[42] (Supplementary Fig. 5a). Deletion of *Rb* in lineages labelled with anti-MSHα generates intermediate lobe tumours in 100% of cases but no anterior lobe tumours[22,43]. In 6-week-old mice, T_c of *Rb$^{-/-}$* anti-MSHα-labelled cancer-resistant anterior lobe cells was 45 h versus 25 h in cancer-prone intermediate lobe cells, and at 10 weeks, T_c was 96 h in the anterior lobe versus 32 h in the intermediate lobe (Fig. 5a). T_s was also higher in anterior lobe cells (Fig. 5a). Thus, T_c predicts cancer susceptibility in *Rb$^{-/-}$* pituitary regardless of whether *Rb* is deleted at four or eight weeks of age.

Neuroendocrine cells represent less than 0.5% of lung epithelium but aggressively form multiple small cell lung cancers (SCLCs) in all mice after loss of *Rb* and *p53*, and despite being orders of magnitude more abundant, lung AT2 and club cells are far less prone to developing into tumours[44,45]. Multiple *Rb$^{-/-}$* lung cells divide ectopically[46], so neuroendocrine cells are uniquely highly prone to cancer. To assess T_c in *Rb*- and *p53*-deficient lungs, we fed pregnant *hSPC-rtTA;tet-cre;Rb$^{f/f}$;p53$^{f/f}$* mice with doxycycline from plug detection to birth. Endogenous SPC (also known as PSPC) is specifically expressed in AT2 cells, but the transgene expresses rtTA throughout lung epithelium, causing ubiquitous *tet*-Cre induction and SCLC that is lethal within five to six months[46,47]. We confirmed SCLC lesions in *Rb$^{-/-}$;p53$^{-/-}$* lung by P60 (Supplementary Fig. 5c). Ki67 labelling confirmed ectopic division in embryonic day 18 (E18) neuroendocrine (CGRP$^+$), AT2 (SPC$^+$) or club (CCSP$^+$) cells (Supplementary Fig. 5c), and cancer-prone neuroendocrine cells had the lowest proliferation index (Extended Data Fig. 6b). Despite this, quadruple labelling (examples in Supplementary Fig. 5d) revealed T_c values of 22 h and 42 h in AT2 and club cells, respectively, but only 11 h in cancer-prone neuroendocrine cells (Fig. 5b, left). Thus, relative T_c also predicts cancer susceptibility in *Rb$^{-/-}$;p53$^{-/-}$* lung.

To assess adult lung, we generated *creERT2;LSL-tdTomato;Rb$^{f/f}$;p53$^{f/f}$* mice or control *creERT2;LSL-tdTomato* littermates. We added tamoxifen at four weeks of age, then performed EdU–BrdU labelling at eight weeks and collected the lung. In total, 50–70% of neuroendocrine, AT2 or club cells were labelled with tdTomato (Extended Data Fig. 7a), Ki67 labelling confirmed ectopic division (Supplementary Fig. 5e), and although proliferation index was 0–3% in tdTomato$^+$ or tdTomato$^-$ cells of control mice or in tdTomato$^-$ cells of *creERT2;LSL-tdTomato;Rb$^{f/f}$;p53$^{f/f}$* mice, it increased to 11%, 10% or 8% in tdTomato$^+$ *Rb*- and *p53*-knockout neuroendocrine, AT2 and club cells, respectively (Extended Data Fig. 7a). Quadruple labelling (Supplementary Fig. 5f) revealed T_c values of 33.8 h, 60.4 h and 71.3 h in neuroendocrine, AT2 and club cells, respectively, whereas S phase durations were similar across these cell types (Fig. 5b, right). Therefore, relative T_c predicts the cancer-prone lung lineage independently of initiation event timing.

Next, to extend these studies beyond *Rb* mutations, we assessed KRAS, which, similar to RB, regulates many cancer hallmarks (https://cancer.sanger.ac.uk/cosmic/census-page/KRAS). In contrast to the *Rb$^{-/-}$;p53$^{-/-}$* lung, *Kras* activation transforms AT2, but not neuroendocrine cells, generating adenocarcinoma[6]. To assess T_c, we used a Cre-activated *Kras^{G12D}* allele[48]. *creERT2;LSL-tdTomato;Kras^{G12D}* mice or control *creERT2;LSL-tdTomato* littermates were treated with tamoxifen at four weeks of age, and then two weeks later, EdU–BrdU labelling was applied and the lungs were collected. Nascent tdTomato$^+$ tumours were positive for SPC (AT2 cells) but negative for CGRP (also known as CGRP1) and CCSP (also known as uteroglobin) (Supplementary Fig. 6a) even though 50%–80% of AT2, neuroendocrine and club cells were tdTomato$^+$ (Extended Data Fig. 7b, left). In tamoxifen-treated mice, the proliferation index in tdTomato$^+$ or tdTomato$^-$ cells of control mice or

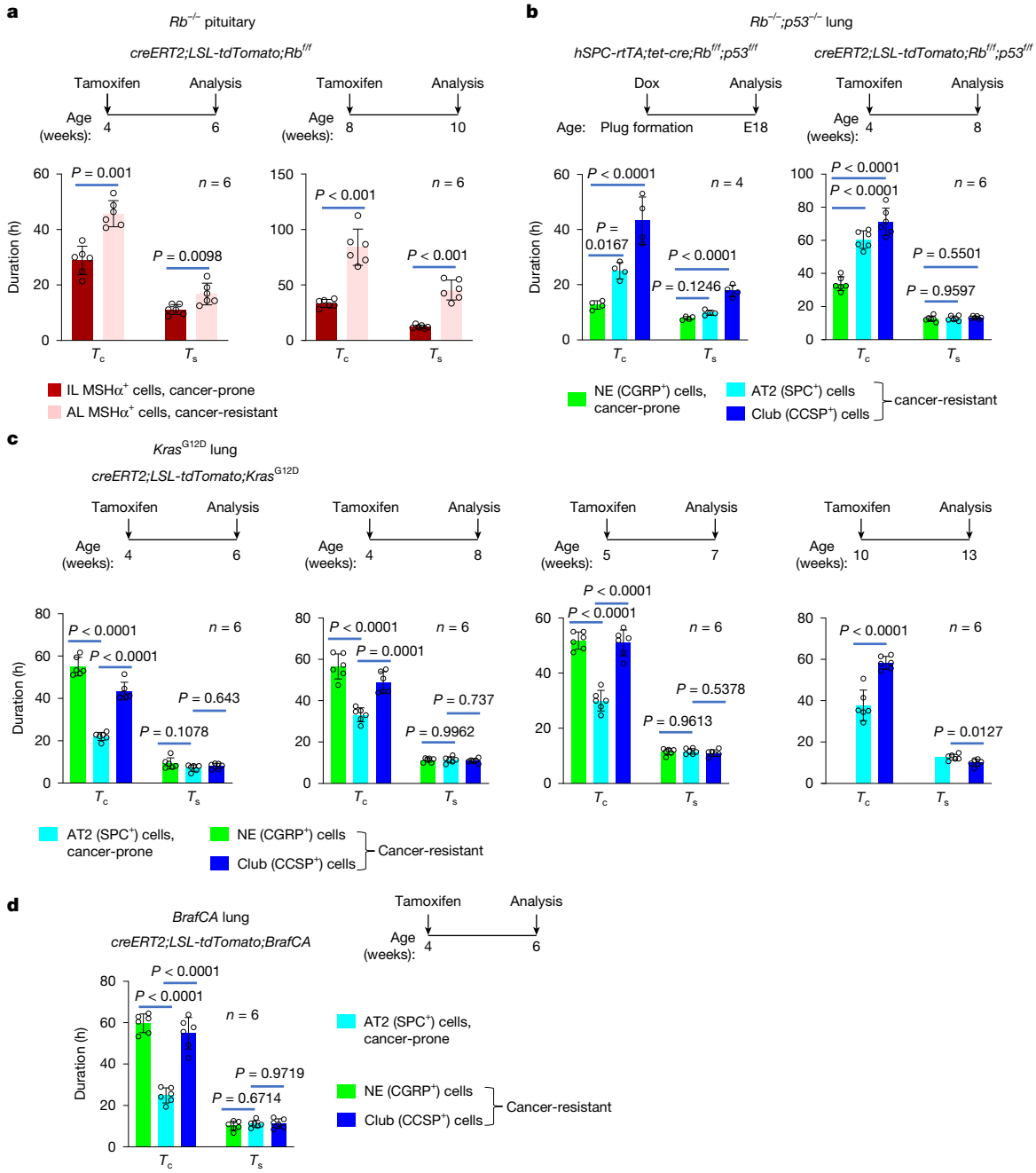

Fig. 5 | Shortest T_c as a general hallmark of cancer susceptibility. a, T_c and T_s of MSHα+ cells in the intermediate (IL) and anterior (AL) pituitary lobes of *Rb*-null (*creERT2;LSL-tdTomato;Rb*$^{f/f}$) mice injected with tamoxifen at 4 or 8 weeks of age and assessed at 6 or 10 weeks of age, respectively. **b**, T_c and T_s of lung CGRP+ neuroendocrine (NE), SPC+ AT2 and CCSP+ club cells from mice that are deficient in *Rb* and *p53* (*hSPC-rtTA;tet-cre;Rb*$^{f/f}$*;p53*$^{f/f}$) that were injected with doxycycline (Dox) at plug formation and assessed at E18, and from *Rb*- and *p53*-deficient (*creERT2;LSL-tdTomato;Rb*$^{f/f}$*;p53*$^{f/f}$) mice injected with tamoxifen at 4 weeks of age and assessed at 8 weeks of age. **c**, T_c and T_s of lung NE, AT2 and club cells of *Kras*^{G12D} (*creERT2;Kras*^{G12D}*;LSL-tdTomato* mice) mice injected with tamoxifen at 4 weeks, 4 weeks, 5 weeks or 10 weeks of age and assessed at 6 weeks, 8 weeks, 7 weeks or 13 weeks of age, respectively. **d**, T_c and T_s of lung NE, AT2 and club cells of *Braf*^{CA} (*creERT2;LSL-tdTomato;Braf*^{CA}) mice that were injected with tamoxifen at 4 weeks of age and assessed at 6 weeks of age. Data are mean ± s.d. ($n = 6$ mice (**a**, **b** (right), **c**, **d**); $n = 4$ mice (**b** (left)) per group as indicated). Exact *P* values for the comparison between MSHα+ intermediate lobe versus anterior lobe cells (**a**), NE versus AT2 or club cells (**b**) or AT2 versus NE or club cells (**c**,**d**) by one-way ANOVA with Bonferroni correction (**b**, **c** (first three graphs), **d**) or two-tailed unpaired *t*-test (**a**, **c** (right)) are shown.

tdTomato− cells of *creERT2;LSL-tdTomato;Kras*^{G12D} mice was 0–5%, but increased to 14%, 20%, and 11% in tdTomato+ *Kras*^{G12D}-expressing neuroendocrine, AT2 and club cells, respectively (Extended Data Fig. 7b.). Quadruple labelling (Supplementary Fig. 6b,c) revealed T_c values of 21 h, 58 h and 43 h in *Kras*^{G12D}-expressing AT2, neuroendocrine and club cells, respectively, whereas T_s values in these cells were similar (Fig. 5c, left). Thus, cancer-prone AT2 cells had the shortest relative T_c.

Next, we varied the timing of *Kras* activation and the incubation period. We activated *Kras* at 4, 5 or 10 weeks of age and assessed T_c 4, 2 or 3 weeks later, respectively. As before, Cre was efficiently activated (indicated by tdTomato+ expression) and *Kras*^{G12D} induction at four or five weeks of age triggered ectopic division in neuroendocrine, AT2 and club cells, whereas induction at ten weeks of age caused division of AT2 and club cells, but not neuroendocrine cells (Extended Data

Fig. 7c–e). Regardless of the timing of *Kras* activation, T_c was always shortest in cancer-prone AT2 cells (Fig. 5c).

Finally, we tested a different Ras pathway component. KRAS binds and activates the BRAF serine/threonine kinase, and constitutively active BRAF(V600E) (BRAF(CA), encoded by the $Braf^{CA}$ allele) generates adenomas from AT2 cells, but not neuroendocrine or club cells[5]. We generated *creERT2;LSL-tdTomato;*$Braf^{CA}$ mice, and following tamoxifen treatment at four weeks of age observed tdTomato$^+$ lesions arising from AT2 (SPC$^+$) cells two weeks later (Supplementary Fig. 7a). Tamoxifen induced tdTomato expression in 50–80% of cells, and ectopic division to similar levels in neuroendocrine, AT2 and club cells in mice with the $Braf^{CA}$ allele (Extended Data Fig. 7f). Quadruple labelling (Supplementary Fig. 7b) revealed a similar T_s across lineages, and T_c was 24.8 h, 59.7 h and 54.8 h in AT2, neuroendocrine and club cells, respectively (Fig. 5d). Thus, regardless of how the Ras pathway is activated in lung, cancer-prone cells exhibit the shortest relative T_c. In summary, among many surviving lineages, the shortest T_c marks the most cancer-prone lineage in all tested cancer models independent of tissue type (retina, pituitary and lung), oncogenic driver (*Rb* and *p107* inactivation, *Rb* inactivation, *Rb* and *p53* inactivation, *Kras* activation or *Braf* activation) or initiation event timing, and for different cancers arising from distinct cells of origin in the same tissue (SCLC in *Rb*- and *p53*-deficient neuroendocrine cells and non-small cell lung cancer (NSCLC) in *Kras*- or *Braf*-activated AT2 cells).

Discussion

Although transformation captures the most attention, oncogenic mutations are harmless in most lineages and are common in cancer-free human tissues[1]. Chimeric studies provide notable examples of the abundant contribution of 'initiated' cells to cancer-free adult tissues. Thus, normal development, rather than cell death, senescence or immune clearance, is a widespread, yet poorly understood mechanism of tumour evasion[2–4]. Cancer genes are usually associated with the function to which they were first assigned (for example, cell cycle for *Rb*, cytoplasmic signal transduction for Ras genes, and development for *Wnt1* or *Notch1*), but affect multiple cancer hallmarks, explaining why they are so commonly mutated. Given the complexity of cancer initiation, it was unclear whether any one hallmark would predict cancer susceptibility in cells that survive oncogenic lesions across multiple cancers. However, we find here that T_c distinguishes cancer-prone from resistant lineages in tumours initiated by different oncogenic events. First, we found that the cell of origin of $Rb^{-/-}$;$p107^{-/-}$ retinoblastoma has a shorter T_c (26 h) than cancer-resistant lineages (over 77 h). Moreover, mutations that block retinoblastoma increased the T_c of the cell of origin. Notably, weaker tumour-suppressing mutations (such as $Cdk2^{-/-}$, 33 h) had a less potent effect on T_c than those that completely blocked tumorigenesis (such as $Skp2^{+/-}$, 45 h). This rule held in cancer-prone lineages in $Rb^{-/-}$ pituitary and $Rb^{-/-}$;$p53^{-/-}$ lung. T_c also predicted lung cancer susceptibility following *Kras* or *Braf* mutation. Studies in pituitary and lung revealed that T_c predicts outcome independently of the timing of the oncogenic event. The lung data are particularly revealing, since despite causing ectopic division in the same lineages, the cells of origin of *Rb* and Ras pathway cancers are distinct, and T_c was predictive in both circumstances. Further studies are needed to determine the extent to which this correlation holds across other tissues and oncogenic events, but our work explains how many cell types escape cancer without deploying senescence, apoptosis or immune surveillance[1–4].

Our study began with suppression of retinoblastoma, which we expected to affect many cancer hallmarks. Indeed, $Skp2^{-/-}$ induced senescence, rescued polarity and decreased proliferation index. However, although $Skp2^{+/-}$ suppressed tumorigenesis with similar potency, it did not affect any of the eight hallmarks assessed. $p27^{KI/KI}$ induced senescence, but did not rescue polarity or affect other hallmarks, and none of the other *p27* or *Cdk2* or combined *Cdk1* and *Cdk2* manipulations affected any of the tested hallmarks. Remarkably, cancer could be suppressed without altering cell death, senescence, immune infiltration, DNA damage, angiogenesis, apical polarity, differentiation or proliferation index. It is remarkable that a tissue with so many cancerous defects can resist transformation. Thus, cancer has many hallmarks, but they do not necessarily cause cancer. T_c may need to fall below a critical threshold, which varies with context, to synergize with other cancer hallmarks to enable tumorigenesis.

Our results do not minimize the importance of other hallmarks to initiation: alone, a short T_c is insufficient for tumorigenesis, because normal cells can divide rapidly—for example, T_c in the E6.5–E7.5 mouse embryo is 5–7 h in epiblast and less than 3 h in the proliferative zone[49]. Our results show that whereas relative T_c reveals cancer susceptibility in one set of circumstances (*Rb*- and *p107*-deficient retina, *Rb*-deficient pituitary, *Rb*- and *p53*-deficient lung, *Kras*-activated lung and *Braf*-activated lung), it does not predict susceptibility across different initiation events or tissues. For example, the T_c in cancer-prone $Kras^{G12D}$ AT2 cells (21 h) was similar to the T_c in cancer-resistant $Rb^{-/-}$;$p53^{-/-}$ AT2 cells (22 h). Thus, T_c is prognostic in a single context (one initiation event, one tissue), but not between contexts (different initiation events or tissues). To use a behavioural analogy, T_c resembles a self-control score[50]: between two groups in different settings that are exposed to a particular stress or temptation (initiation event), absolute score alone could not predict who would lose control, because it also depends on circumstances; however, the score could predict this effect within one group in one setting. The complexity underlying neoplastic transformation underscores the predictive power of T_c across in vivo settings.

When CDK2 activity is reduced upon exit from M phase, cells in G1 cells with the lowest CDK2 activity do not re-enter S phase[51]; shorter T_c may therefore reflect higher CDK2 activity in this G1 trough. Cells with insufficient CDK2 activity would eventually cease dividing and never form tumours. Notably, CDK2 phosphorylates and inhibits transcription factors that promote differentiation and cell cycle exit[27], and CDK1 and CDK2 phosphorylate epigenetic regulators that influence S phase re-entry[52,53]. Unlike T_c, T_s did not predict cancer-prone lineages, but future work will delineate whether effects on G1, G2 and/or M phase determine T_c; CDK2 also regulates general transcription through the C-terminal domain of RNA polymerase II, a quarter of CDK2 targets are transcriptional regulators, and a gene expression signature accurately tracks CDK2 activity[26,37,54–56].

The observation that varying T_c may block cancer initiation suggests it may be possible to reduce cancer incidence in high-risk cohorts with occasional treatments to expand short cell cycles in initiated clones. Indeed, drug-based cell cycle inhibition can reduce retinoblastoma or colon cancer initiation[23,57] and a threshold of CDK activity appears to be critical in the early stages of multiple human cancers[37]. Elegant non-toxic methods exist to inhibit CDKs without perturbing normal division[58]. Chemoprevention trials have been performed in high-risk groups, especially smokers[59,60], and similar trials to increase T_c in initiated cells may promote cell cycle exit, mimicking the beneficial cul-de-sac in ectopically dividing but cancer-resistant lineages.

Online content

Any methods, additional references, Nature Portfolio reporting summaries, source data, extended data, supplementary information, acknowledgements, peer review information; details of author contributions and competing interests; and statements of data and code availability are available at https://doi.org/10.1038/s41586-025-08935-x.

1. Yizhak, K. et al. RNA sequence analysis reveals macroscopic somatic clonal expansion across normal tissues. *Science* **364**, eaaw0726 (2019).
2. Maandag, E. C. et al. Developmental rescue of an embryonic-lethal mutation in the retinoblastoma gene in chimeric mice. *EMBO J.* **13**, 4260–4268 (1994).
3. Williams, B. O. et al. Extensive contribution of Rb-deficient cells to adult chimeric mice with limited histopathological consequences. *EMBO J.* **13**, 4251–4259 (1994).

4. Wang, Z. Q., Grigoriadis, A. E., Möhle-Steinlein, U. & Wagner, E. F. A novel target cell for c-Fos-induced oncogenesis: development of chondrogenic tumours in embryonic stem cell chimeras. *EMBO J.* **10**, 2437–2450 (1991).
5. Dankort, D. et al. A new mouse model to explore the initiation, progression, and therapy of BRAFV600E-induced lung tumors. *Genes Dev.* **21**, 379–384 (2007).
6. Kwon, M. & Berns, A. Mouse models for lung cancer. *Mol. Oncol.* **7**, 165–177 (2013).
7. Mainardi, S. et al. Identification of cancer initiating cells in K-Ras driven lung adenocarcinoma. *Proc. Natl Acad. Sci. USA* **111**, 255–260 (2014).
8. Gibson, P. et al. Subtypes of medulloblastoma have distinct developmental origins. *Nature* **468**, 1095–1099 (2010).
9. He, M. et al. Intrinsic apoptosis shapes the tumor spectrum linked to inactivation of the deubiquitinase BAP1. *Science* **364**, 283–285 (2019).
10. de Bruin, A. et al. Rb function in extraembryonic lineages suppresses apoptosis in the CNS of Rb-deficient mice. *Proc. Natl Acad. Sci. USA* **100**, 6546–6551 (2003).
11. Wu, L. et al. Extra-embryonic function of Rb is essential for embryonic development and viability. *Nature* **421**, 942–947 (2003).
12. Dannenberg, J. H., Schuijff, L., Dekker, M., van der Valk, M. & te Riele, H. Tissue-specific tumor suppressor activity of retinoblastoma gene homologs p107 and p130. *Genes Dev.* **18**, 2952–2962 (2004).
13. Costa, C., Paramio, J. M. & Santos, M. Skin tumors Rb(eing) uncovered. *Front. Oncol.* **3**, 307 (2013).
14. Ehmer, U. et al. Organ size control is dominant over Rb family inactivation to restrict proliferation in vivo. *Cell Rep.* **8**, 371–381 (2014).
15. Hanahan, D. & Weinberg, R. A. Hallmarks of cancer: the next generation. *Cell* **144**, 646–674 (2011).
16. Chen, D. et al. Cell-specific effects of RB or RB/p107 loss on retinal development implicate an intrinsically death-resistant cell-of-origin in retinoblastoma. *Cancer Cell* **5**, 539–551 (2004).
17. MacPherson, D. et al. Cell type-specific effects of Rb deletion in the murine retina. *Genes Dev.* **18**, 1681–1694 (2004).
18. Ajioka, I. et al. Differentiated horizontal interneurons clonally expand to form metastatic retinoblastoma in mice. *Cell* **131**, 378–390 (2007).
19. Chen, D. et al. Rb-mediated neuronal differentiation through cell-cycle-independent regulation of E2f3a. *PLoS Biol.* **5**, e179 (2007).
20. Zhou, Y. et al. Rb is required for retinal angiogenesis and lamination. *Cell Death Dis.* **9**, 370 (2018).
21. Wei, R. et al. Rb1/Rbl1/Vhl loss induces mouse subretinal angiomatous proliferation and hemangioblastoma. *JCI Insight* **4**, 127889 (2019).
22. Wang, H. et al. Skp2 is required for survival of aberrantly proliferating Rb1-deficient cells and for tumorigenesis in *Rb1*$^{+/-}$ mice. *Nat. Genet.* **42**, 83–88 (2010).
23. Sangwan, M. et al. Established and new mouse models reveal E2f1 and Cdk2 dependency of retinoblastoma, and expose effective strategies to block tumor initiation. *Oncogene* **31**, 5019–5028 (2012).
24. Cai, Z. et al. The Skp2 pathway: a critical target for cancer therapy. *Semin. Cancer Biol.* **67**, 16–33 (2020).
25. Sharma, S. S. & Pledger, W. J. The non-canonical functions of p27^{Kip1} in normal and tumor biology. *Cell Cycle* **15**, 1189–1201 (2016).
26. Lim, S. & Kaldis, P. Cdks, cyclins and CKIs: roles beyond cell cycle regulation. *Development* **140**, 3079–3093 (2013).
27. Hardwick, L. J. A., Azzarelli, R. & Philpott, A. Cell cycle-dependent phosphorylation and regulation of cellular differentiation. *Biochem. Soc. Trans.* **46**, 1083–1091 (2018).
28. Massacci, G., Perfetto, L. & Sacco, F. The cyclin-dependent kinase 1: more than a cell cycle regulator. *Br. J. Cancer* **129**, 1707–1716 (2023).
29. Aleem, E., Kiyokawa, H. & Kaldis, P. Cdc2–cyclin E complexes regulate the G1/S phase transition. *Nat. Cell Biol.* **7**, 831–836 (2005).
30. Martin, A. et al. Cdk2 is dispensable for cell cycle inhibition and tumor suppression mediated by p27^{Kip1} and p21^{Cip1}. *Cancer Cell* **7**, 591–598 (2005).
31. Ortega, S. et al. Cyclin-dependent kinase 2 is essential for meiosis but not for mitotic cell division in mice. *Nat. Genet.* **35**, 25–31 (2003).
32. Santamaria, D. et al. Cdk1 is sufficient to drive the mammalian cell cycle. *Nature* **448**, 811–815 (2007).
33. Chen, D., Chen, Y., Forrest, D. & Bremner, R. E2f2 induces cone photoreceptor apoptosis independent of E2f1 and E2f3. *Cell Death Differ.* **20**, 931–940 (2013).
34. Lin, H. K. et al. Skp2 targeting suppresses tumorigenesis by Arf–p53-independent cellular senescence. *Nature* **464**, 374–379 (2010).
35. Wu, J. et al. Skp2 E3 ligase integrates ATM activation and homologous recombination repair by ubiquitinating NBS1. *Mol. Cell* **46**, 351–361 (2012).
36. Pearson, J. D. et al. Binary pan-cancer classes with distinct vulnerabilities defined by pro- or anti-cancer YAP/TEAD activity. *Cancer Cell* **39**, 1115–1134.e12 (2021).
37. McCurdy, S. R., Pacal, M., Ahmad, M. & Bremner, R. A CDK2 activity signature predicts outcome in CDK2-low cancers. *Oncogene* **36**, 2491–2502 (2017).
38. Pacal, M. & Bremner, R. Mapping differentiation kinetics in the mouse retina reveals an extensive period of cell cycle protein expression in post-mitotic newborn neurons. *Dev. Dyn.* **241**, 1525–1544 (2012).
39. Das, G., Choi, Y., Sicinski, P. & Levine, E. M. Cyclin D1 fine-tunes the neurogenic output of embryonic retinal progenitor cells. *Neural Dev.* **4**, 15 (2009).
40. Jin, K. et al. Tfap2a and 2b act downstream of Ptf1a to promote amacrine cell differentiation during retinogenesis. *Mol. Brain* **8**, 28 (2015).
41. Nikitin, A. Y., Juárez-Pérez, M. I., Li, S., Huang, L. & Lee, W. H. RB-mediated suppression of spontaneous multiple neuroendocrine neoplasia and lung metastases in *Rb*$^{+/-}$ mice. *Proc. Natl Acad. Sci. USA* **96**, 3916–3921 (1999).
42. Harno, E., Gali Ramamoorthy, T., Coll, A. P. & White, A. POMC: the physiological power of hormone processing. *Physiol. Rev.* **98**, 2381–2430 (2018).
43. Vooijs, M., van der Valk, M., te Riele, H. & Berns, A. Flp-mediated tissue-specific inactivation of the retinoblastoma tumor suppressor gene in the mouse. *Oncogene* **17**, 1–12 (1998).
44. Sutherland, K. D. et al. Cell of origin of small cell lung cancer: inactivation of *Trp53* and *Rb1* in distinct cell types of adult mouse lung. *Cancer Cell* **19**, 754–764 (2011).
45. Yang, D. et al. Intertumoral heterogeneity in SCLC is influenced by the cell type of origin. *Cancer Discov.* **8**, 1316–1331 (2018).
46. Wikenheiser-Brokamp, K. A. Rb family proteins differentially regulate distinct cell lineages during epithelial development. *Development* **131**, 4299–4310 (2004).
47. Akeno, N. et al. TRP53 mutants drive neuroendocrine lung cancer through loss-of-function mechanisms with gain-of-function effects on chemotherapy response. *Mol. Cancer Ther.* **16**, 2913–2926 (2017).
48. Johnson, L. et al. Somatic activation of the *K-ras* oncogene causes early onset lung cancer in mice. *Nature* **410**, 1111–1116 (2001).
49. Snow, M. H. L. Gastrulation in the mouse: growth and regionalization of the epiblast. *Development* **42**, 293–303 (1977).
50. Manapat, P. D., Edwards, M. C., MacKinnon, D. P., Poldrack, R. A. & Marsch, L. A. A psychometric analysis of the brief self-control scale. *Assessment* **28**, 395–412 (2021).
51. Spencer, S. L. et al. The proliferation–quiescence decision is controlled by a bifurcation in CDK2 activity at mitotic exit. *Cell* **155**, 369–383 (2013).
52. Michowski, W. et al. Cdk1 controls global epigenetic landscape in embryonic stem cells. *Mol. Cell* **78**, 459–476.e13 (2020).
53. Chi, Y. et al. A novel landscape of nuclear human CDK2 substrates revealed by in situ phosphorylation. *Sci. Adv.* **6**, eaaz9899 (2020).
54. Chi, Y. et al. Identification of CDK2 substrates in human cell lysates. *Genome Biol* **9**, R149 (2008).
55. Deng, L., Ammosova, T., Pumfery, A., Kashanchi, F. & Nekhai, S. HIV-1 Tat interaction with RNA polymerase II C-terminal domain (CTD) and a dynamic association with CDK2 induce CTD phosphorylation and transcription from HIV-1 promoter. *J. Biol. Chem.* **277**, 33922–33929 (2002).
56. Nekhai, S. et al. HIV-1 Tat-associated RNA polymerase C-terminal domain kinase, CDK2, phosphorylates CDK7 and stimulates Tat-mediated transcription. *Biochem. J.* **364**, 649–657 (2002).
57. Boquoi, A., Chen, T. & Enders, G. H. Chemoprevention of mouse intestinal tumorigenesis by the cyclin-dependent kinase inhibitor SNS-032. *Cancer Prev. Res. Phila.* **2**, 800–806 (2009).
58. Hydbring, P. et al. Cell-cycle-targeting microRNAs as therapeutic tools against refractory cancers. *Cancer Cell* **31**, 576–590.e8 (2017).
59. New, M. & Keith, R. Early detection and chemoprevention of lung cancer. *F1000Res* **7**, 61 (2018).
60. Sporn, M. B. & Lippman, S. in *Holland-Frei Cancer Medicine* (eds Kufe, D. W. et al.) Ch. 30 (BC Decker, 2003).
61. Huang, R. et al. The NCATS BioPlanet – an integrated platform for exploring the universe of cellular signaling pathways for toxicology, systems biology, and chemical genomics. *Front. Pharmacol.* **10**, 445 (2019).

Methods

Mouse strains and genotyping

All animal experiments were performed according to institutional and national guidelines approved by the Toronto Centre for Phenogenomics (TCP) and Cincinnati Children's Hospital Medical Center. Mice were housed under controlled conditions (specific-pathogen free, 12 h:12 h light:dark cycle, 19–22 °C, 45–65% humidity) with ad libitum access to food and water. We added environmental enrichment in the form of plastic tunnels and nesting material to all the cages. Clinical symptoms define the welfare of animals. That includes visible masses, any degree of reduced mobility/distress, weight loss or evidence of haemorrhage. Humane intervention points are set based on institutional standard operating procedure (SOP) of Humane Intervention Point Guidelines and Cancer Models–Humane Intervention Point Guidelines. In brief, tumour size exceeding 1,700 mm^3 in adult mice is considered the endpoint for cancer models. No mouse exceeded the humane endpoints stipulated in our animal SOPs. Both male and female mice were used in the study.

α-cre mice (P. Gruss, age E14–P400), *B6.129P2(Cg)-Braf*^{tm1Mmcm}*/J* (Jackson Laboratory, strain 017837, common name: *BRaf*^{CA}, age P0–P42), *B6.Cg-Gt(ROSA)26Sortm14(CAG-tdTomato)*$^{Hze/J}$, also known as *Ai14(tdTomato)* (Jackson Laboratory, strain 007914, age P0–P91), *B6.129-Gt (ROSA)26Sortm1(cre/ERT2)*$^{Tyj/J}$ (Jackson Laboratory, strain 008463, age P0–P91), *B6.129S4-Kras*$^{tm4Tyj/J}$ (Jackson Laboratory, strain 008179, age P0–P91), *Cdk1*$^{f/f}$ (D. Santamaria and M. Barbacid, age P0–P400), *Cdk2*$^{f/f}$ (D. Santamaria and M. Barbacid, age P0–P400), *p107*$^{-/-}$ mice (M. Rudnicki, age P0–P400), *p27*$^{CK-/CK-}$ mice (A. Besson and J. Roberts, age P0–P400), *p27*^{T187A} (A. Besson and J. Roberts, age P0–P400), *p53*$^{f/f}$ mice (A. Berns, age E18–P56), *Rb*$^{f/f}$ mice (A. Berns, age E14–P400), *Skp2*$^{-/-}$ mice (K. Nakayama, age P0–P400), *SPC-rtTA* (Whitsett, age E18–P60), *TetO-Cre* (Whitsettage age E18–P60) and *Z/Red* (Jackson Laboratory, strain 005438, age E16) mice were maintained on a mixed background. Different genotypes were compared within the same litter and at least four to six litters. We have not noted any phenotypic differences in separate litters. Genotyping was performed as before and per The Jackson Laboratory guidelines using established primers (Supplementary Table 6).

α-cre retinoblastoma model

α-cre mice[62] were mated with *Rb*$^{f/f}$ mice[63,64] and *p107*$^{-/-}$ mice[65] to generate *α-cre; Rb*$^{f/f}$*;p107*$^{-/-}$ (*Rb/p107* DKO) mice, an established retinoblastoma mouse model[16]. DKO mice were further mated with *Skp2*$^{-/-}$ (ref. 66), *Cdk1*$^{f/f}$ (ref. 32), *Cdk2*$^{f/f}$ (ref. 67), *p27*$^{CK-}$ (ref. 68) and *p27*^{T187A} (*p27*^{KI})[69] mice to elucidate the mechanism of tumorigenesis. Genotypes were determined by PCR using established primers (Supplementary Table 6). *p107*$^{-/-}$ littermates were used as controls.

Doxycycline-induce *Rb* and *p53* double-knockout SCLC model

SPC-rtTA transgenic mice[70] and *tet-OCre* transgenic mice[46,47,71] were mated to *Rb*$^{f/f}$ mice[63,64] and *p53*$^{f/f}$ mice[72], to generate *SPC-rtTA;tet-OCre;Rb*$^{f/f}$*;p53*$^{f/f}$ mice, an established SCLC animal model[47]. Genotypes were determined by PCR analysis using established primers[46,73] (Supplementary Table 6). Gestational age was assigned by vaginal plug date designated embryonic day (E) 0.5. A 50× doxycycline stock solution (50 mg ml^{-1} in 50% ethanol) was freshly prepared prior to each administration of drug and diluted in water or in PBS for injection. Dams were treated with 125 μg doxycycline (Sigma, D9891) in 0.5 ml PBS by intraperitoneal injection on E0.5–E1.5 and administered doxycycline in the drinking water at a final concentration of 1.0 mg ml^{-1}. Doxycycline water was replaced three times per week because of the light sensitivity of doxycycline.

Tamoxifen-induced *Rb* and *p53* double-knockout SCLC model

Rosa-creERT2 and *Ai14 (tdTomato)* transgenic mice were mated to *Rb*$^{f/f}$ (refs. 63,64) and *p53*$^{f/f}$ mice[72] to generate *creERT2;tdTomato;Rb*$^{f/f}$*;p53*$^{f/f}$ mice, an established SCLC animal model[47]. Genotypes were determined by PCR analysis using established primers[46,73] (Supplementary Table 6). *creERT2;tdTomato* littermate mice were used as control. Both *creERT2; tdTomato;Rb*$^{f/f}$*;p53*$^{f/f}$ mice and control mice were treated with 100 mg kg^{-1} body weight Tamoxifen (Sigma, T5468) in 0.45 ml corn oil (Sigma, C8267) once by intraperitoneal injection on P28, and the lung was collected 4 weeks later.

Tamoxifen-induced *Rb*-knockout pituitary cancer model

Rosa-creERT2 and *Ai14 (tdTomato)* transgenic mice were mated to *Rb*$^{f/f}$ mice[63,64] to generate *creERT2;tdTomato;Rb*$^{f/f}$ mice. Genotypes were determined by PCR analysis using established primers (Supplementary Table 6). *tdTomato;Rb*$^{f/f}$ littermate mice were used as control. Both *creERT2;tdTomato;Rb*$^{f/f}$ mice and control mice were treated with 100 mg kg^{-1} body weight Tamoxifen (Sigma, T5468) in 0.45 ml corn oil (Sigma, C8267) once by intraperitoneal injection on P28 or P56, and the pituitary was collected 2 weeks later.

Tamoxifen-induced *Kras*^{G12D} NSCLC model

Rosa-creERT2 and *Ai14* (tdTomato) transgenic mice were mated to *LSL-Kras*^{G12D} mice to generate *creERT2;tdTomato;Kras*^{G12D} mice. *Kras*^{G12D} mice is a well-established NSCLC mouse model[48]. Genotypes were determined by PCR analysis using established primers (Supplementary Table 6). *creERT2;tdTomato* littermate mice were used as control. To optimize tamoxifen treatment to obtain ectopic division of multiple cell types we treated these mice with 7 doses (0.1, 1, 2.5, 25, 50, 100, 250 mg kg^{-1} body weight). For 0.1–25 mg kg^{-1} doses, the overall percent of tdTomato$^+$ cells correlated with dosage but reached a plateau using at higher levels. However, while 0.1–50 mg kg^{-1} doses induced ectopic division of Spc$^+$ AT2 cells, it did not induce ectopic cell division of Cgrp$^+$ neuroendocrine cells and Ccsp$^+$ club cells, but both 100 and 250 mg kg^{-1} doses induced ectopic cell division all three cell types. We used the 100 mg kg^{-1} dose in this study. Both *creERT2;tdTomato; Kras*^{G12D} mice and control mice were treated once with 100 mg kg^{-1} body weight Tamoxifen (Sigma, T5468) in 0.45 ml corn oil (Sigma, C8267) by intraperitoneal injection at the indicated age, and lung was collected 2–4 weeks later, as indicated.

Tamoxifen-induced *Braf*^{CA} model

Rosa-creERT2 and *Ai14 (tdTomato)* transgenic mice were mated to *Braf*^{CA} mice to generate *creERT2;tdTomato;Braf*^{CA} mice. Genotypes were determined by PCR analysis using established primers (Supplementary Table 6). *creERT2;tdTomato* littermate mice were used as controls. Both *creERT2;tdTomato;Braf*^{CA} mice and control mice were treated once with 100 mg kg^{-1} body weight Tamoxifen (Sigma, T5468) in 0.45 ml corn oil (Sigma, C8267) by intraperitoneal injection at 4 weeks of age, and the lung was collected 2 weeks later.

Staggered EdU–BrdU labelling

For cell cycle duration analysis, animals were injected subcutaneously once with EdU (Sigma, 900584. 30 μg per g of body weight) to label all cells in S phase (DKO retina at P8, *Rb*$^{-/-}$ pituitary at 4 or 6 weeks of age; *Rb*$^{-/-}$*;p53*$^{-/-}$ lung at E18 and 8 weeks of age; *Kras*^{G12D} lung at 6, 7, 8 and 13 weeks of age, *Braf*^{CA} lung at 6 weeks of age). After 2.5 h, BrdU (Sigma, B5002. 100 μg per g of body weight) was injected once subcutaneously. Tissues were collected 0.5 h after BrdU injection, fixed in 4% paraformaldehyde for 1 h (eyes) or 2 h (pituitary, lung) and dehydrated in 30% sucrose for 24 h.

Histology, immunofluorescence and measurements

All collected mouse tissues were embedded in OCT (TissueTek 4583), frozen on dry ice and cut into 12–14 μm sections on Superfrost slides. For S phase labelling, BrdU$^+$ cells were detected using a rat anti-BrdU antibody (Abcam, ab6326, 1:500) or a mouse monoclonal antibody (DSHB, G3G4, 1:1,000). EdU$^+$ cells were detected using Click-iT EdU Alexa Fluor 555

Imaging Kit (Life technologies, C10338). Other antibodies were active caspase-3 (Cell Signaling Technology, 9661,1:500), AP2A (Santa Cruz, SC-8975, 1:500), aPKCι (BD Transduction lab, 610176, 1:500), ARR3 (Millipore, AB15282, 1:500), BRN3 (Santa Cruz, SC-6062, 1:500), calretinin (Santa Cruz, SC-11644,1:500), CCSP (Seven Hills Bioreagent, WRAB-3950, 1:1,000), CGRP (Sigma, C8198, 1:1,000), CRX (C. Y. Gregory-Evans, 1:500), cyclin A2 (Abcam, Ab181591, 1:500), cyclin B1 (Cell Signaling Technology, 4138S, 1:500), galectin 3 (Santa Cruz, SC-19283, 1:500), Ki67 (BD science Pharmingen, 550609, 1:500; ThermoFisher Scientific, 14-5698-82, 1:500), MSHA (Fisher Scientific, AB508MI, 1:200), MYCN (Santa Cruz, SC-791, 1:500), N-cadherin (Santa Cruz, SC7939, 1:500), OC2 (R&D systems, AB6294, 1:500), P21^{cip1} (Abcam, ab188224, 1:500), p27 (BD Biosciences, 554069, 1:500), phospho-aPKCι/λ (ThermoFisher, 44-968 G, 1:500), phospho-histone H3 (Santa Cruz, SC-8656, 1:500), PKCα (Sigma, P5704, 1:500), PTF1A (Pierre Cordelier, INSERM, France, 1:200), rhodopsin (Santa Cruz, SC-57433, 1:500) and SOX9 (EMD Millipore, MAB5535, 1:500),Spc (Abcam, ab40879, 1:1,000).

Validation of the primary antibodies is provided on the manufacturer's websites or in the referenced citations: antigen retrieval was performed as described[19] by boiling sections in citric acid (H-3300, Vector Lab) or Target Retrieval Solution (S1699, Agilent). Primary antibodies or labelled cells were visualized using donkey anti-mouse, donkey anti-rabbit, donkey anti-rat and donkey anti-goat antibodies conjugated with Alexa-488, Alexa-568 or Alexa-647 (1:1,000; Molecular Probes), or donkey anti-mouse IgG H&L (Alexa Fluor 405) (Abcam, ab175658), DyLight 405 AffiniPure donkey anti-rat IgG (H + L) (Jackson ImmunoResearch, 712-475-153). F-actin was labelled by Alexa Fluor 488 Phalloidin (ThermoFisher Scientific, A12379) or Alexa Fluor 568 Phalloidin (ThermoFisher Scientific, A12380). Nuclei were counter-stained with 4, 6-diamidino-2-phenyindole (DAPI; Sigma).

Labelled cells were visualized and images captured with a Nikon Eclipse Ti or Ti2 laser scanning confocal microscope. Retinal thickness measurements were performed with Nikon NIS-Elements AR 3.10 software. Quantification used horizontal retinal sections containing the optic nerve, and lung/pituitary gland sections, and were analysed with ImageJ (https://imagej.nih.gov/ij/). At least 3 sections per sample and 4–6 samples from different litters were counted.

For whole-mount retinal staining, eyeballs were enucleated and incubated for 30 min in 4% paraformaldehyde. The retinas were incubated at 4 °C with FITC-conjugated IB4 (Sigma L2895) and DAPI in PBS for 1–2 days. After brief washes with PBS, radial cuts were made to divide the retina into 4 quadrants to flatten the retina, and the tissue was mounted with Mowiol. For vascular blood vessel analysis, representative images were analysed with AngioTool (https://ccrod.cancer.gov/confluence/display/ROB2/Home) to assess the vessel covered area (%), average vessel length and mean E lacunarity of the vascular plexus. In brief, at least three 200× magnification images (320 × 320μm field of view per retina) per eye and 6 eyes from the same genotypes of different litters were counted. To compare the vascular density of the DKO retina to the control, we used vascular images taken from a similar depth below the GCL to represent the IVP and DVP for the DKO retina.

Whole-mount F-actin staining

E16 or P0 eyeballs were enucleated and incubated for 30 min in 4% paraformaldehyde in PBS. With a dissection microscope, a circumferential incision was made around the limbus, followed by removal of the anterior segment, lens and vitreous body. The retinas were incubated with Alexa Fluor 488 Phalloidin (ThermoFisher Scientific, A12379, 1:500) or Alexa Fluor 568 Phalloidin (ThermoFisher Scientific, A12380, 1:500) and DAPI in PBS for overnight. After brief PBS washes, radial cuts were made to divide the retina into four quadrants to flatten the retina, and flat retinas were mounted with Mowiol. Immunofluorescent staining was analysed with the Nikon Eclipse Ti laser scanning confocal microscope. The whole retinal area and polarity-defect area were measured with the microscope program.

Senescence-associated β-galactosidase staining

Frozen horizontal retinal sections were stained for β-galactosidase at pH 6.0 using the senescence-associated β-galactosidase staining kit (Cell Signaling, 9860) according to the manufacturer's guidelines. In brief, 120 μl staining solution was added to each slide, cover-slipped and sealed with rubber cement. The slide boxes were placed in a sealed humid container in a 37 °C dry incubator (no CO_2) and incubated for 1–2 days. Colour images were taken with an Olympus BX61 microscope. Positive cells/sections were counted under the Olympus BX61 microscope. For each genotype, at least six retinas were analysed. For each retina, at least three representative sections were counted.

Immune cell detection

P8 eyeballs of *p107*$^{-/-}$, *α-cre;Rb*$^{f/f}$*;p107*$^{-/-}$ and *α-cre;Rb*$^{f/f}$*;p107*$^{-/-}$*;Skp2*$^{+/-}$ mice were enucleated, and peripheral retinas were dissected in fresh cold HBSS. Dissected peripheral retinas were transferred to 200 μl of cold HBSS per retina. An equivalent amount of Papain solution was added and incubated at 37 °C for 10 min, and the tube inverted gently every 2 min. Next, the digestion solution was discarded by pipetting without disturbing the retina. Mechanical trituration of the retina was performed in 600 μl of neurobasal medium supplemented with 10% FBS by pipetting slowly 10 to 15 times with a P1000 pipette tip. Samples were then DNAse treated for 5 min at 37 °C. Cell suspensions were centrifuged using a swing-bucket rotor at 200*g* for 5 min. The supernatant was carefully aspirated off the cell pellet, and the pellet was suspended in 1–5 ml neurobasal medium with 1% FBS. Cellular aggregates were removed by straining cells through a 50-μm cell strainer (pluriSelect). Splenocytes were collected by grinding a *p107*$^{-/-}$ mouse spleen through a 40-μm mesh, and then red blood cells (RBC) were removed by incubating cells for 10 min in RBC lysis buffer (Sigma, 11814389001).

To stain for immune markers, the dissociated retinal cells or splenocytes were washed in FACS buffer (PBS + 1% FBS) and then blocked with mouse Fc block (BD 553141, 1 μg per 10^6 cells) for 10 min on ice. After washing with FACS buffer, 4×10^5 cells in 200 μl FACS buffer were stained with phycoerythrin (PE) or allophycocyanin (APC)-conjugated anti-B220 (0.5 μg, 12-0452-81), anti-CD3 (0.75 μg, 17-0032-80), anti-CD335/NKp46 (0.75 μg, 12-3351-80), anti-CD45 (0.1 μg, 12-0451-82), anti-CD11b (0.25 μg, 17-0112-81) or appropriate isotype control antibodies (all from ThermoFisher) for 30 min on ice then washed with FACS buffer. Samples were analysed using a Gallios flow cytometer and Kaluza analysis software (Beckman Coulter). Dead cells were excluded using FxCycle violet DNA dye (ThermoFisher). The gating strategy is provided in Supplementary Fig. 8.

Measurement of cell cycle duration

Similar to a prior method[39], animals were subject to staggered EdU/BrdU labelling and tissues were collected and fixed (as detailed above). For retinal sections, EdU was detected with the Click-iT EdU Alexa Fluor 647 Imaging Kit first, then co-labelled with antibodies against BrdU (mouse anti-BrdU antibody, DSHB, G3G4), Ki67 (rat antibody, ThermoFisher Scientific, 14-5698-82) to label all dividing cells, and cell-type-specific markers including mature amacrine cells (AP2a), amacrine precursors (PTF1A), Müller glia (SOX9), horizontal cells (OC2), and predominantly neuronal retinal precursors (p21^{cip1} and MYCN). Matching a prior report[74], staining retinal sections from mice subject only to EdU labelling confirmed that the G3G4 mouse anti-BrdU antibody does not cross-react with EdU.

For lung and pituitary sections, EdU was specifically detected using the Click-iT EdU Alexa Fluor 647 Imaging Kit first, followed by an EdU-blocking procedure to prevent cross-reaction with rat anti-BrdU antibody[75] (Abcam, ab6326). In brief, after EdU was detected using the Click-iT EdU Alexa Fluor 647 Imaging Kit, slides were treated with 2 mM azidosulfide (Sigma, 244546) in the Click-iT buffers for 30 min. Staining sections from mice subject only to EdU labelling confirmed that the

anti-BrdU antibody did not cross-react with EdU. After the EdU-blocking procedure, slides were co-labelled with antibodies against BrdU (rat anti-BrdU antibody, Abcam, ab6326), Ki67 (mouse antibody, BD science Pharmingen 550609) to label all dividing cells, and cell-type-specific markers including lung neuroendocrine cells (CGRP, rabbit, Sigma, C8198), lung club cells (CCSP, rabbit, Seven Hills Bioreagents, WRAB-3950), lung alveolar type II cells (SPC, rabbit, Abcam, ab40879), and pituitary melanotropes in the intermediate lobe and corticotropes in the anterior lobe (MSHA, Fisher Scientific, AB508MI), and imaged by confocal microscopy.

ImageJ (Fiji, version 1.54g) was used to manually count EdU/BrdU-labelled cells in 60× images using the image\color\channels tool. For cell-specific cell cycle data, we first counted the number of cell types of interest (for example, $CGRP^+$ neuroendocrine cells). Next (or first in cases where no cell type-specific marker was used), we added the Ki67 channel to count dividing cells ($CGRP^+$; $Ki67^+$), then we added the EdU channel to count how many dividing cells were EdU-positive ($CGRP^+$; $Ki67^+$; EdU^+). Next, we added the BrdU channel to count how many dividing cells were BrdU-positive ($CGRP^+$; $Ki67^+$; $BrdU^+$). After that, we combined EdU and BrdU data with Marker/Ki67 to count $marker^+Ki67^+BrdU^-EdU^+$ cells. Counting each image was performed three times to ensure accuracy. Functions used to calculate T_c and T_s are illustrated and explained in detail in Supplementary Fig. 3. All the raw counts used in T_c and T_s calculations are provided in Supplementary Table 7. Examples of images used for counts are provided in Supplementary Figs. 4–7.

The number of EdU^+;$BrdU^-$ cells forms the denominator of T_c and T_s calculations (Supplementary Fig. 3), thus if some of these cells divide this denominator would increase, artificially decreasing T_c and T_s. Prior publications assume that no or very few EdU-labelled cells divide, and that the EdU-only cells have reached G2/M but not beyond. We performed additional assays to examine this assumption.

First, we labelled P8 *Rb/p107* DKO mice with EdU for 1 h, 1.5 h, 2 h, 3 h, 4 h, 5 h or 6 h, then stained retinal sections for EdU, phospho-histone H3 (PH3) and DAPI (Supplementary Fig. 9a). H3 phosphorylation begins in late G2 with chromosomal condensation, but is most prominent in early-mid M phase, and H3 dephosphorylation commences in late anaphase/early telophase[76], thus PH3 is widely used as a late G2/M marker. If G2/M was <3 h, all cells in S phase at the time of EdU labelling would have reached M phase by then, and the EdU^+ cells that were labelled in early-mid S phase would continue to enter G2/M at later times (S phase in DKO P8 retina is ~25 h, Fig. 4c), ensuring a long plateau of 100% EdU^+;$PH3^+$ double-labelled cells beyond 3 h. Conversely, if G2/M is >3 h, only a fraction of $PH3^+$ cells would also be EdU^+, which would continue to rise with time, eventually reaching the 100% plateau. As expected, the fraction of $PH3^+$ cells that were also EdU^+ increased over time, confirming the movement of prior S phase cells through G2 into M (Supplementary Fig. 9b). No double-labelled cells were detected at 1 h or 1.5 h, a tiny fraction was seen at 2 h, which continued to increase only reaching 100% at 6 h. At 3 h, the time point used in our T_c measurement studies, only 23.9% of $PH3^+$ cells were EdU^+ (Supplementary Fig. 9b). These data suggest that 3 h is insufficient for EdU-labelled cells in the P8 DKO retina to divide.

Second, we also performed EdU/PH3/DAPI triple labelling in sections from *Rb* pituitary, *Rb/p53* lung, *Kras* lung, and *Braf* lung cancer models used in the paper (Supplementary Fig. 9c). The fraction of M phase cells that were EdU^+ after 3 h was ~30–50%, similar in range to the DKO retina, and well below the 100% expected if EdU^+ cells could complete mitosis in 3 h (Supplementary Fig. 9d). Thus, 3 h also appears insufficient for EdU-labelled cells to divide in these cancer models.

Third, as an additional test in retina, P8 DKO mice were exposed to EdU at 0 h, then BrdU from 2.5–3 h and retinal sections were stained for EdU. A cocktail of three rabbit antibodies targeting cyclin A2, cyclin B1, and PH3 to label S, all G2 and all M phase cells (Supplementary Fig. 9e). Any EdU-only cells that traverse M into G1 would be EdU^+ but negative for all the other markers (cyclin A2, mid/late S phase and G2; cyclin B1, G2 and early M phase; PH3, late G2 and M phase). Notably, all the EdU^+ cells co-labelled with the A2/B1/PH3 antibody mix, and no cells were positive only for EdU (Supplementary Fig. 9f). This result confirms that EdU-labelled cells do not divide in a 3 h window.

Single-cell RNA sequencing

Retinal dissociation. P8 eyeballs of *α-cre;*$Rb^{f/f}$*;*$P107^{-/-}$ (DKO, tumour-prone) and *α-cre;*$Rb^{f/f}$*;*$P107^{-/-}$*;*$Skp2^{+/-}$ (DKO-$Skp2^{+/-}$, tumour-resistant) mice were enucleated, and peripheral retinas (*α-cre* expression areas) were dissected in fresh and cold HBSS. Dissected peripheral retinas were then transferred to 200 µl of cold HBSS per retina. An equivalent amount of Papain solution (for 1 ml, 700 µl reagent grade water, 100 µl of freshly prepared 50 mM L-cysteine (Sigma), 100 µM 10 mM EDTA, 10 µM 60 mM 2-mercaptoethanol (Sigma), and Papain added to 1 mg ml^{-1} (Worthington)) was added and incubated at 37 °C for 10 min, the tube was inverted gently every 2 min during the incubation. After the incubation steps, the digestion solution was discarded by pipetting without disturbing the retina. Mechanical trituration of the retina was performed in 600 µl of neurobasal medium supplemented with 10% FBS by pipetting slowly 10 to 15 times with a P1000 pipette tip. Samples then were subjected to DNAse treatment (5 µl DNAse I (RNAse-free Recombinant DNAse I; Roche) for every 1 ml of dissociation solution) for 5 min at 37 °C. Cell suspensions were then centrifuged using a swing-bucket rotor at 200*g* for 5 min. The supernatant was carefully aspirated off the cell pellet, then resuspended in 1–5 ml neurobasal medium with 1% FBS. Cellular aggregates were removed by straining cells through a 50-µm cell strainer (pluriSelect).

Single-cell library preparation and sequencing. Single-cell gene expression libraries were prepared using the Single Cell 3′ Reagent Kit v2 (10x Genomics) according to the manufacturer's protocol. Libraries were sequenced using the HiSeq3000 (Illumina) with the 10x Gene Expression recommended parameters (read 1, 28 cycles and read 2, 100 cycles).

CellRanger pre-processing. Raw data were processed through the CellRanger pipelines (10x Genomics, V2.2.0). For each run of DKO and DKO-$Skp2^{+/-}$ genotypes, reads were quantified into UMI gene–barcode matrix using the mouse reference index provided by 10x Genomics (refdata-cellranger-mm10) and default parameters of the count pipeline to filter out low-quality cell barcodes. This process resulted in 3,621 estimated cells with an average of 52,983 reads and a median of 2,884 genes per cell for the DKO sample and 5,196 estimated cells with an average of 31,520 reads and a median of 1,873 genes per cell for the DKO-$Skp2^{+/-}$ sample. Then, matrices for individual runs were aggregated together into a single gene–barcode matrix with the CellRanger's aggr pipeline to avoid artefacts that may be introduced due to differences in sequencing depth when comparing the two genotypes. The aggregation kept 74.3% reads from the DKO sample and 100% reads from the DKO-$Skp2^{+/-}$ sample and ended with 8,817 estimated cells with an average of 34,749 reads and a median of 1,941 genes per cell.

Identification of non-retinal cell types. The cloupe files generated by CellRanger were viewed using the 10x Genomics Loupe Browser and cells in clusters were explored by their over-expressed genes and expression of typical retinal, immune and astrocyte cell marker genes. We defined clusters as immune for their outstanding expression of marker genes *Aif1* and *Lgals9*, and astrocyte cells by marker gene *Aqp4*. The proportions of immune and astrocyte cells in total cells were compared between DKO and DKO-$Skp2^{+/-}$ genotypes. For further analysis of retina cells, these non-retinal cells were excluded.

Quality control and normalization. After removing non-retinal cells, data was further processed and analysed mainly by Scanpy Python

toolkit (https://github.com/scverse/scanpy) and Seurat R toolkit (https://github.com/satijalab/seurat). For downstream analysis, low-expression genes and poor-quality cells were further filtered out from each single-cell dataset. After filtering, only genes expressed in >3 cells and cells expressing >500 genes and less than 15% of mitochondrial genes were retained, with 3,501 cells in DKO and 5,019 cells in DKO-*Skp2*$^{+/-}$ dataset. The retained data were normalized, and log-transformed by Scanpy's normalize-total and log1p, respectively. The aggregated data were filtered by only keeping the cells retained in each individual sample after the above filtering and genes with >10 counts in total. This resulted in 8,520 cells, including 5,019 DKO-*Skp2*$^{+/-}$ and 3,501 DKO retinal cells, and 15,731 genes. Then the aggregated data were normalized and log-transformed following the same methods as above.

Assigning cell cycle phases. To identify cycling cells and the effect of cell cycle heterogeneity on the data, each cell was assigned cell cycle scores and phases using Scanpy's function score_genes_cell_cycle. A list of cell cycle marker genes, including markers for S and G2M phase[77] were used for the scoring, which calculates the difference of mean expression of the given cell cycle genes and the mean expression of randomly selected reference genes from binned gene pools that match the distribution of the given genes' expression. The human gene names were converted to mouse gene names by biomaRt package. Based on its cell cycle scores, a cell is predicted to be in G2M, S or G1 phase. Cells expressing neither S nor G2M genes are likely not cycling (G0) or in G1 phase.

Detection of doublets. To detect if any cells were grouped together as a cluster by artefacts of the problematic doublets or multiplets, where two or more cells receive the same barcode and result in a hybrid transcriptome, the python package "scrublet"[78] was used to calculate doublet score and predicted doublets for each sample and possible artefact clusters by default parameters and expected doublets rate—DKO, 0.03; and DKO-*Skp2*$^{+/-}$, 0.04—based on the number of captured cells. Raw data matrices for each individual sample were used for this analysis. The annotation of the detected doublets for cells were transferred onto the aggregated data.

Clustering and identifying major retinal cell components. To minimize the effects of cell cycle heterogeneity and to emphasize clustering based on genes related to cell lineage, the cell cycle was regressed from the previous normalized expression matrix. Both scores for G2M and S phase were regressed out with the regress_out function of Scanpy. After scaling, the top 2,000 highly variable genes were selected for the principal component analysis to reduce the dimension of data. The neighbourhood graph of cells was computed with the top 50 principal components, and then, the graph was embedded into two dimensions using UMAP. Cell clusters were identified by the Leiden graph-clustering method[79], which directly clustering the neighbourhood graph of cells.

To annotate the retinal cell identity of each cluster, we associated the clusters with retinal cell types based on scores of known retinal cell-type-specific genes (Extended Data Fig. 4h). The scores of each cell type were calculated for each cell using the Scanpy's score_genes function with the same algorithm of the score_genes_cell_cycle. A cluster was assigned to a cell type with the highest average score and percentage of cells detected with positive scores within the cluster. The cell-type annotated clusters were further refined and verified by highly differential expressed genes for each cluster. The DEGs were identified for each cluster against the rest of the clusters using the rank_genes_group function with Wilcoxon rank-sum test. Of them, marker genes for each cluster were further filtered by the filter_rank_genes_groups function with default parameters. Expression of the top 10 marker genes for each cluster were compared between mouse normal retinal development and these samples by UMAP visualization. Using the normal mouse retina development scRNA-seq data[80] As a reference, we also identified each individual cell for its cell type with the ingest function of Scanpy, which fit a model on the reference data and used it to project new data with cell annotations. This mapping was applied using data for each individual sample, and mapped cell types were transferred to the aggregated data. The cell cycle effects were regressed out from the reference data and genotype data before mapping.

Top genes that distinguished particular cell types included: *Apoe*, Müller glia cluster (Mu); *Rom1*, photoreceptors (PR); *Ebf1*, amacrine precursors (AmP); *Pcsk1n*, mature amacrine cells (AmM); *Fbxo5*, rare remaining mitotic progenitors (ProgM); *Isl1*, bipolar cells (BiP); and *Otx2, Neurod1* and *Neurod4*, neurogenic (Neu) cluster[80–86] (Fig. 3b, Extended Data Fig. 4g and Supplementary Table 2).

Differential gene expression between two genotypes within each cluster. To identify DEGs between two genotypes within each cluster, the function FindMarkers from the Seurat package was used with the MAST test for two condition comparisons. Significant DEGs were selected as those with adjusted *P* values less than 0.1, average $\log_2$ fold change higher than 0.25 and percentage (proportion) of cells with expression within a cluster larger than 0.1. The enrichment of CDK2-associated genes[37] and cell cycle genes expressed in S and G2M phases in the DEGs were evaluated by the hypergeometric test phyper in R. The Bioplanet terms enriched in the DEGs were also identified using the online tool Enrichr (https://maayanlab.cloud/Enrichr/)[87].

Western blotting

Peripheral mouse retinas were homogenized with a 30-gauge needle 5–10 times in 1× cell lysis buffer (Cell Signaling 9803) with 0.1 mM PMSF, 1μg ml^{-1} aprotinin and 1μg ml^{-1} leupeptin. Proteins were separated by SDS–PAGE, transferred to nitrocellulose membrane, and analysed using ODYSSEY Infrared Imaging System (LI-COR) with antibodies against active caspase-3 (Cell Signaling Technology 9661, 1:200), p27 (554069, BD Biosciences, 1:200), SKP2 (SC-74477; Santa Cruz, 1:1,000) and β-actin (A5441, Sigma, 1:2,000).

Statistical analysis

Sample sizes were chosen based on power analysis and common practice in mouse experiments. Sample sizes (n) were estimated by the formula $n = [2(Z_{\alpha} + Z_{1-\beta})^2]/\mathrm{SES}^2$. Type I error ($\alpha$) is set as 0.05, type II error (β) is set as 10–20% and is a two-sided effect. The SES (Cohen's d) is the standardized effect size, equal to the ES (effect size) divided by the pooled s.d., so it is the magnitude of the difference between the means of two groups in s.d. units[88]. For animal experiments, SES of 1.1×, 1.5× and 2.0× s.d. are suggested to represent small, moderate and significant responses, respectively[88]. According to the formula above, 4–7 mice are required to detect effect with 80% power, and 6–10 mice are needed to detect effects with 90% power. Thus, 4 or more typically 6 mice were used for each experiment to detect impact with 80–90% power. All data are presented as mean ± s.d. Kaplan–Meier survival curves and statistical analysis were performed using GraphPad Prism software. An unpaired Student's *t*-test was used to compare two groups. One-way ANOVA followed by Bonferroni correction was used for multiple comparisons. The *P* values for Kaplan–Meier curves were calculated using the log-rank (Mantel–Cox) test.

Reporting summary

Further information on research design is available in the Nature Portfolio Reporting Summary linked to this article.

Data availability

Data files for transcriptomic scRNA-seq analyses are available at the Gene Expression Omnibus (GEO) under accession GSE245137. Mouse

reference index provided by 10x Genomics (refdata-cellranger-mm10) can be downloaded from https://www.10xgenomics.com/support/software/cell-ranger-arc/downloads. All other data are available in the main text or supplementary materials. Source data are provided with this paper.

62. Marquardt, T. et al. Pax6 is required for the multipotent state of retinal progenitor cells. *Cell* **105**, 43–55 (2001).
63. Vooijs, M. & Berns, A. Developmental defects and tumor predisposition in Rb mutant mice. *Oncogene* **18**, 5293–5303 (1999).
64. Vooijs, M., te Riele, H., van der Valk, M. & Berns, A. Tumor formation in mice with somatic inactivation of the retinoblastoma gene in interphotoreceptor retinol binding protein-expressing cells. *Oncogene* **21**, 4635–4645 (2002).
65. LeCouter, J. E. et al. Strain-dependent myeloid hyperplasia, growth deficiency, and accelerated cell cycle in mice lacking the Rb-related *p107* gene. *Mol. Cell. Biol.* **18**, 7455–7465 (1998).
66. Nakayama, K. et al. Targeted disruption of *Skp2* results in accumulation of cyclin E and p27Kip1, polyploidy and centrosome overduplication. *EMBO J.* **19**, 2069–2081 (2000).
67. Barrière, C. et al. Mice thrive without Cdk4 and Cdk2. *Mol. Oncol.* **1**, 72–83 (2007).
68. Besson, A. et al. A pathway in quiescent cells that controls $p27^{Kip1}$ stability, subcellular localization, and tumor suppression. *Genes Dev.* **20**, 47–64 (2006).
69. Malek, N. P. et al. A mouse knock-in model exposes sequential proteolytic pathways that regulate $p27^{Kip1}$ in G1 and S phase. *Nature* **413**, 323–327 (2001).
70. Perl, A.-K. T., Tichelaar, J. W. & Whitsett, J. A. Conditional gene expression in the respiratory epithelium of the mouse. *Transgenic Res.* **11**, 21–29 (2002).
71. Perl, A.-K. T., Wert, S. E., Nagy, A., Lobe, C. G. & Whitsett, J. A. Early restriction of peripheral and proximal cell lineages during formation of the lung. *Proc. Natl Acad. Sci. USA* **99**, 10482–10487 (2002).
72. Marino, S., Vooijs, M., van Der Gulden, H., Jonkers, J. & Berns, A. Induction of medulloblastomas in *p53*-null mutant mice by somatic inactivation of *Rb* in the external granular layer cells of the cerebellum. *Genes Dev.* **14**, 994–1004 (2000).
73. Simpson, D. S., Mason-Richie, N. A., Gettler, C. A. & Wikenheiser-Brokamp, K. A. Retinoblastoma family proteins have distinct functions in pulmonary epithelial cells in vivo critical for suppressing cell growth and tumorigenesis. *Cancer Res.* **69**, 8733–8741 (2009).
74. Harris, L., Zalucki, O. & Piper, M. BrdU/EdU dual labeling to determine the cell-cycle dynamics of defined cellular subpopulations. *J. Mol. Histol.* **49**, 229–234 (2018).
75. Liboska, R., Ligasová, A., Strunin, D., Rosenberg, I. & Koberna, K. Most anti-BrdU antibodies react with 2′-deoxy-5-ethynyluridine–the method for the effective suppression of this cross-reactivity. *PLoS ONE* **7**, e51679 (2012).
76. Hendzel, M. J. et al. Mitosis-specific phosphorylation of histone H3 initiates primarily within pericentromeric heterochromatin during G2 and spreads in an ordered fashion coincident with mitotic chromosome condensation. *Chromosoma* **106**, 348–360 (1997).
77. Tirosh, I. et al. Dissecting the multicellular ecosystem of metastatic melanoma by single-cell RNA-seq. *Science* **352**, 189–196 (2016).
78. Wolock, S. L., Lopez, R. & Klein, A. M. Scrublet: computational identification of cell doublets in single-cell transcriptomic data. *Cell Syst.* **8**, 281–291.e9 (2019).
79. Traag, V. A., Waltman, L. & van Eck, N. J. From Louvain to Leiden: guaranteeing well-connected communities. *Sci. Rep.* **9**, 5233 (2019).
80. Clark, B. S. et al. Single-cell RNA-seq analysis of retinal development identifies NFI factors as regulating mitotic exit and late-born cell specification. *Neuron* **102**, 1111–1126.e5 (2019).
81. Amaratunga, A. et al. Apolipoprotein E is synthesized in the retina by Müller glial cells, secreted into the vitreous, and rapidly transported into the optic nerve by retinal ganglion cells. *J. Biol. Chem.* **271**, 5628–5632 (1996).
82. Tsang, S. H. et al. Retinal degeneration in mice lacking the gamma subunit of the rod cGMP phosphodiesterase. *Science* **272**, 1026–1029 (1996).
83. Bascom, R. A. et al. Cloning of the cDNA for a novel photoreceptor membrane protein (rom-1) identifies a disk rim protein family implicated in human retinopathies. *Neuron* **8**, 1171–1184 (1992).
84. Sas, G. Classification of antithrombin III deficiencies–has a new tower of Babel been built? *Thromb. Haemost.* **60**, 530–531 (1988).
85. Reimann, J. D. et al. Emi1 is a mitotic regulator that interacts with Cdc20 and inhibits the anaphase promoting complex. *Cell* **105**, 645–655 (2001).
86. Park, K. U., Randazzo, G., Jones, K. L. & Brzezinski, J. A. Gsg1, Trnp1, and Tmem215 mark subpopulations of bipolar interneurons in the mouse retina. *Invest. Ophthalmol. Vis. Sci.* **58**, 1137–1150 (2017).
87. Chen, E. Y. et al. Enrichr: interactive and collaborative HTML5 gene list enrichment analysis tool. *BMC Bioinform.* **14**, 128 (2013).
88. Festing, M. F. On determining sample size in experiments involving laboratory animals. *Lab. Anim.* **52**, 341–350 (2018).

Acknowledgements The authors thank P. Gruss, A. Berns, M. Rudnicki, K. Nakayama, A. Besson and J. Roberts for mice; C. Y. Gregory-Evans for the CRX antibody; K. Chan for next generation sequencing; M. Parsons for Flow cytometry analysis; and R. Zirngibl for technical assistance. This study was supported by a Canadian Institutes for Health Research grant to R.B. (grant number PJT 173474); a Krembil Foundation, grant to R.B. (grant number 2020-1); a Rankine family fellowship (to D.C.); a National Institutes of Health/National Heart, Lung and Blood Institute to K.A.W.-B. (grant number RO1 HL079193), and an American Cancer Society grant to K.A.W.-B. (grant number RSG-10-194-01-TBG).

Author contributions R.B. conceived the project, D.C. and R.B. designed the study. K.A.W.-B., L.Z., D. Schramek, D. Santamaria, M.B. and P.P.M. provided conceptual input and reagents. D.C. led the tumour work and analysis of all hallmarks, with help from M.S. for generation and initial analysis of some retinal genotypes, S.L. for generation and analysis of the effect of CDK alleles, P.P. for the pituitary cancer model, K.A.W.-B. and N.A. for generation of *hSPC-rtTA;tet-cre;*$Rb^{f/f}$*;* $p53^{f/f}$ lung samples, J.D.P. for immune infiltrate analysis, A.N. for apical polarity data and analysis, J.D.P. and T.Y. for scRNA-seq library generation, K.H. and S.M. for informatics analysis, and M.P. for the retroviral lineage study. D.C. and R.B. drafted, and all authors reviewed and edited the manuscript.

Competing interests The authors declare no competing interests.

Additional information

Supplementary information The online version contains supplementary material available at https://doi.org/10.1038/s41586-025-08935-x.

Correspondence and requests for materials should be addressed to Rod Bremner.

Peer review information *Nature* thanks the anonymous reviewer(s) for their contribution to the peer review of this work. Peer review reports are available.

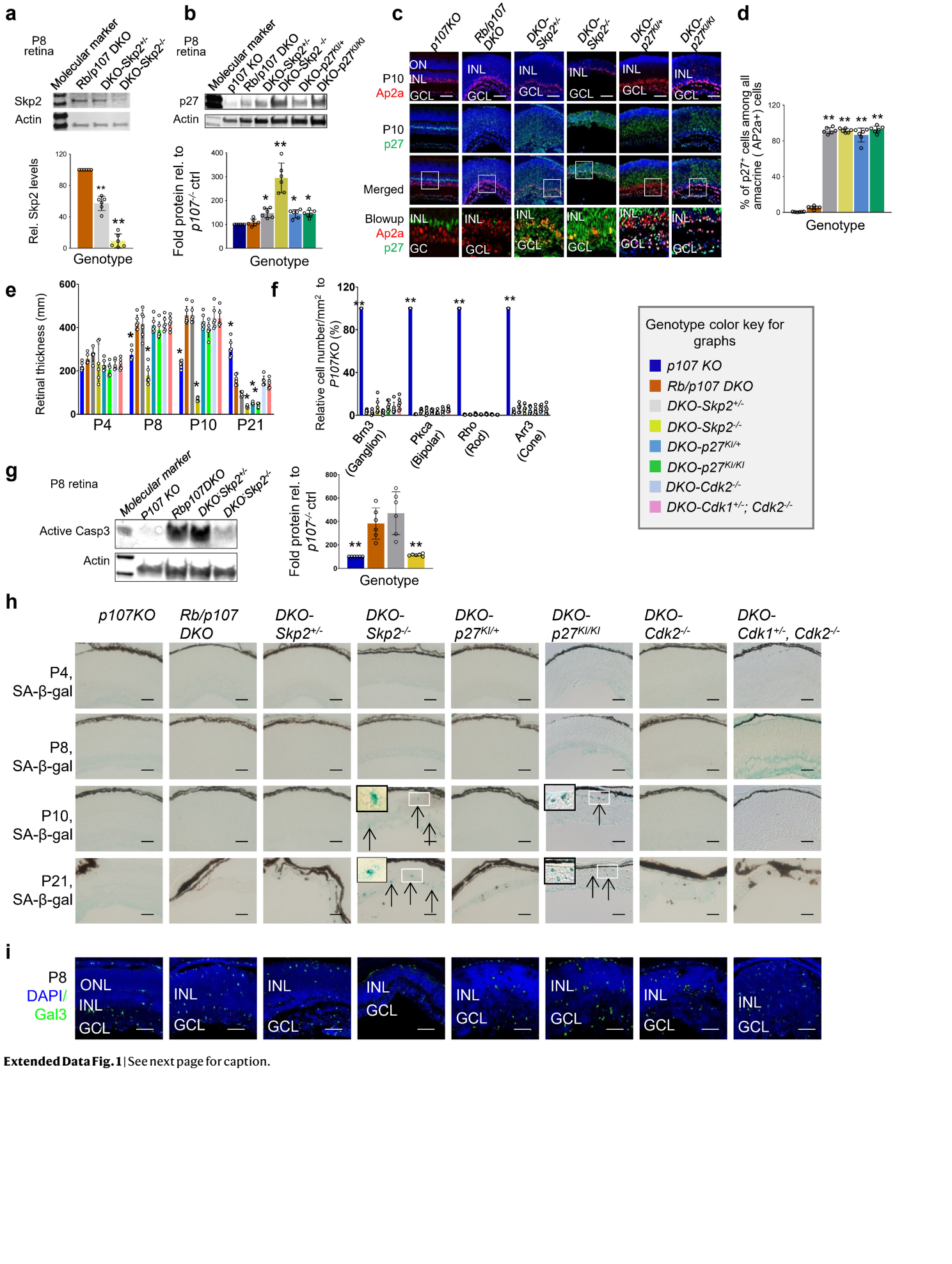

Extended Data Fig. 1 | See next page for caption.

Extended Data Fig. 1 | Disrupting the Skp2-p27-Cdk axis can suppress retinoblastoma without increasing cell death, senescence, or immune infiltration. a) Representative Skp2 Western blot from retinas of the indicated genotypes (upper panel) and quantification (lower panel). **b**) Representative p27 Western blot from P8 retinas of the indicated genotypes (upper panel) and quantification (lower panel). **c**) Horizontal retinal sections from P10 retinas of the indicated genotypes were stained for nuclei (DAPI, blue), p27 (green) and amacrine cells (Ap2a, red). **d**) The percentage of $p27^+$ amacrine ($Ap2a^+$) cells from (c). **e**) Thickness of the retinas of indicated ages and genotypes. **f**) Quantification of $Brn3^+$, $Pkca^+$, $Rhodopsin\ (Rho)^+$ and $Cone\ arrestin\ (Arr3)^+$ cells per mm^2 of P21 retina, normalized to *p107* KO retinas. **g**) Representative active caspase 3 Western blot from P8 retinas of the indicated genotypes (left panel) and quantification (right panel). **h**) Horizontal retinal sections of the indicated ages and genotypes were stained for SA-β-gal. White squares were blown up to show positive SA-β-gal staining (Arrows). **i**) Horizontal P8 retinal sections of the indicated genotypes were stained for nuclei (DAPI, blue) and Galectin-3 (Gal3) to label microglia cells (green). Experiments were repeated independently with similar results at least three times in c, h and i for each animal. Data are presented as mean ± s.d. in a, b, d, e-g from n = 6 mice per cohort as indicated by bars, and asterisks indicate a significant difference between retinas of *DKO* and the indicated genotypes (*, $p < 0.05$; **; $p < 0.01$, one-way ANOVA, Bonferroni correction). Scale bar in c, h, i: 50 µm. ONL: outer nuclear layer. INL: inner nuclear layer. GCL: ganglion cell layer.

Steps to identify a hallmark for susceptibility to oncogenic mutation

1. Discover multiple mutations that suppress cancer
2. Is there a common affected hallmark?
3. Does it distinguish the cancer cell-of-origin from cancer resistant lineages?
4. Is it general? (other cancers and other oncogenic events)

Step 1. Tumor suppressive interventions | **Step 2. Which hallmark does tumor suppression always alter?**

	Cell death	Sene-scence	Immune infiltrate	Abnormal angio-genesis	DNA damage	Disrupted apical polarity	Lineage	Prolif. index	Cell cycle length
Skp2$^{-/-}$	–	✓	–	–	–	✓	NA	✓	✓
Skp2$^{+/-}$	–	–	–	–	–	–	–	–	✓
p27$^{T187A/T187A}$	–	✓	–	–	–	–	NA	–	✓
p27$^{T187A/+}$	–	–	–	–	–	–	NA	–	✓
Cdk2$^{-/-}$	–	–	–	–	–	–	NA	–	✓
Cdk2$^{-/-}$;*Cdk1*$^{+/-}$	–	–	–	–	–	–	NA	–	✓

Key: – Not altered by tumor suppressing mutation ✓ Altered by tumor suppressing mutation

Step 3. Is cell cycle length shorter in retinoblastoma cell-of-origin *vs* resistant lineages?

Resistant lineages	Cell-of-origin	Cell-of-origin with suppressive mutation
77-143 hr	26 hr	109 hr *Skp2*$^{-/-}$ 45 hr *Skp2*$^{+/-}$ 40 hr *p27*$^{KI/+}$ 45 hr *p27*$^{KI/KI}$ 33 hr *Cdk2*$^{-/-}$ 39 hr *Cdk2*$^{-/-}$;*Cdk1*$^{+/-}$
Rb1$^{-/-}$;*p107*$^{-/-}$ *retina*		≥ ~1.2x increase in cell cycle length

Step 4. True for other cancers with other mutations?

Tissue:	Pituitary	Lung	Lung	Lung
Mutation:	*Rb1*$^{-/-}$	*Rb1*$^{-/-}$;*p53*$^{-/-}$	*Kras*^{G12D}	*BrafCA*
Cell-of-origin:	Intermediate lobe cell	Neuroendocrine cell	Alveolar type 2 cell	Alveolar type 2 cell
Shortest cell cycle?:	✓	✓	✓	✓

Extended Data Fig. 2 | An in vivo strategy to identify a cancer cell-of-origin hallmark. The top panel summarizes the four steps. Step 1 introduces mutations to suppress cancer (here, retinoblastoma). Step 2 assesses multiple (here, nine) cancer hallmarks to determine whether any are always altered upon tumor suppression; only cell cycle length (Tc) fulfilled this criterion. Step 3 asks whether Tc is shorter in the cancer-prone (here, amacrine cell) *vs*. cancer-resistant lineages (Müller glia, horizontal cells). Tc in cancer-prone or resistant lineages is indicated on the left, and the effect of multiple tumor-suppressing mutations on Tc is shown on the right. Step 4 compares Tc of cancer-prone *vs*. resistant lineages in multiple other contexts. Tc was always shortest in the cancer-prone lineage independent of oncogenic lesion or tissue (indicated by green check marks).

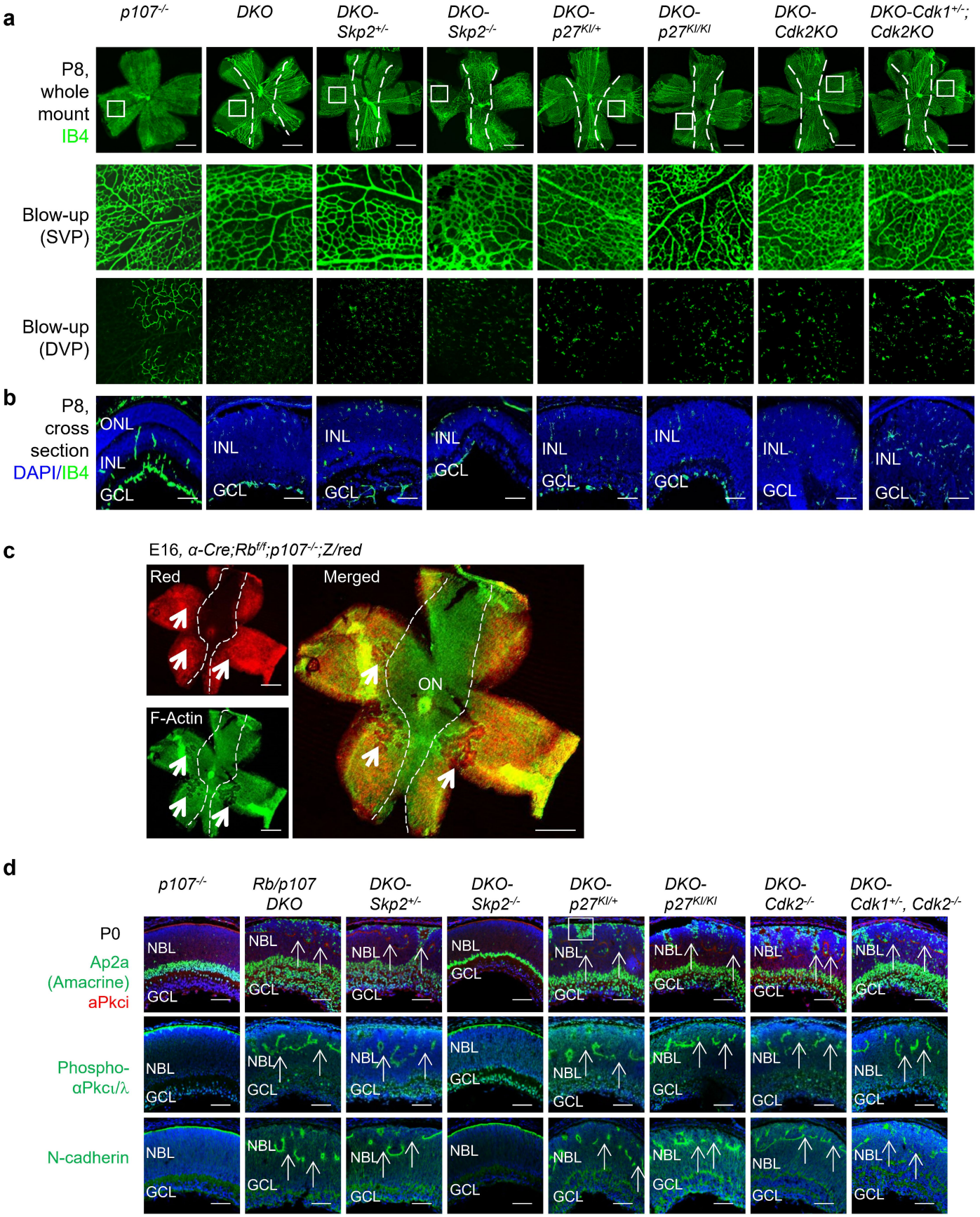

Extended Data Fig. 3 | See next page for caption.

Extended Data Fig. 3 | Tumor suppression without rescuing aberrant angiogenesis and apical polarity. a) IB4 staining of P8 whole-mount retinas of indicated genotypes. Selected areas are blown up to show the superficial vascular plexus (SVP) and deep vascular plexus (DVP). **b**) IB4 (green) and DAPI (blue) staining of P8 retinal sections of indicated genotypes. **c**) E16 whole-mount retina of *αCre;Rb*$^{f/f}$*;p107*$^{-/-}$*;Z/red* mouse stained for F-actin (green). Red fluorescence indicates Cre-activity. Arrows indicate OLM breaks in Cre^{+} region labelled by F-actin. **d**) Horizontal retinal sections from P0 mice of the indicated genotypes were stained for nuclei (DAPI, blue) and amacrine cells (Ap2a, green), or apical polarity complex components (aPkcι, red; phospho-aPkcι/λ: green), or adherens junctions (N-cadherin, green). Arrows as in (c). Dotted lines in a and c indicate the boundary between no α-Cre expression (central retina) and α-Cre expression areas (peripheral retina). Experiments were repeated independently with similar results at least two times in a, b and d for each animal. Scale bars: 50 μm in b, d; 200 μm in a, c. ONL: outer nuclear layer. INL: inner nuclear layer. GCL: ganglion cell layer. NBL: Neuroblast layer. ON: optic nerve head.

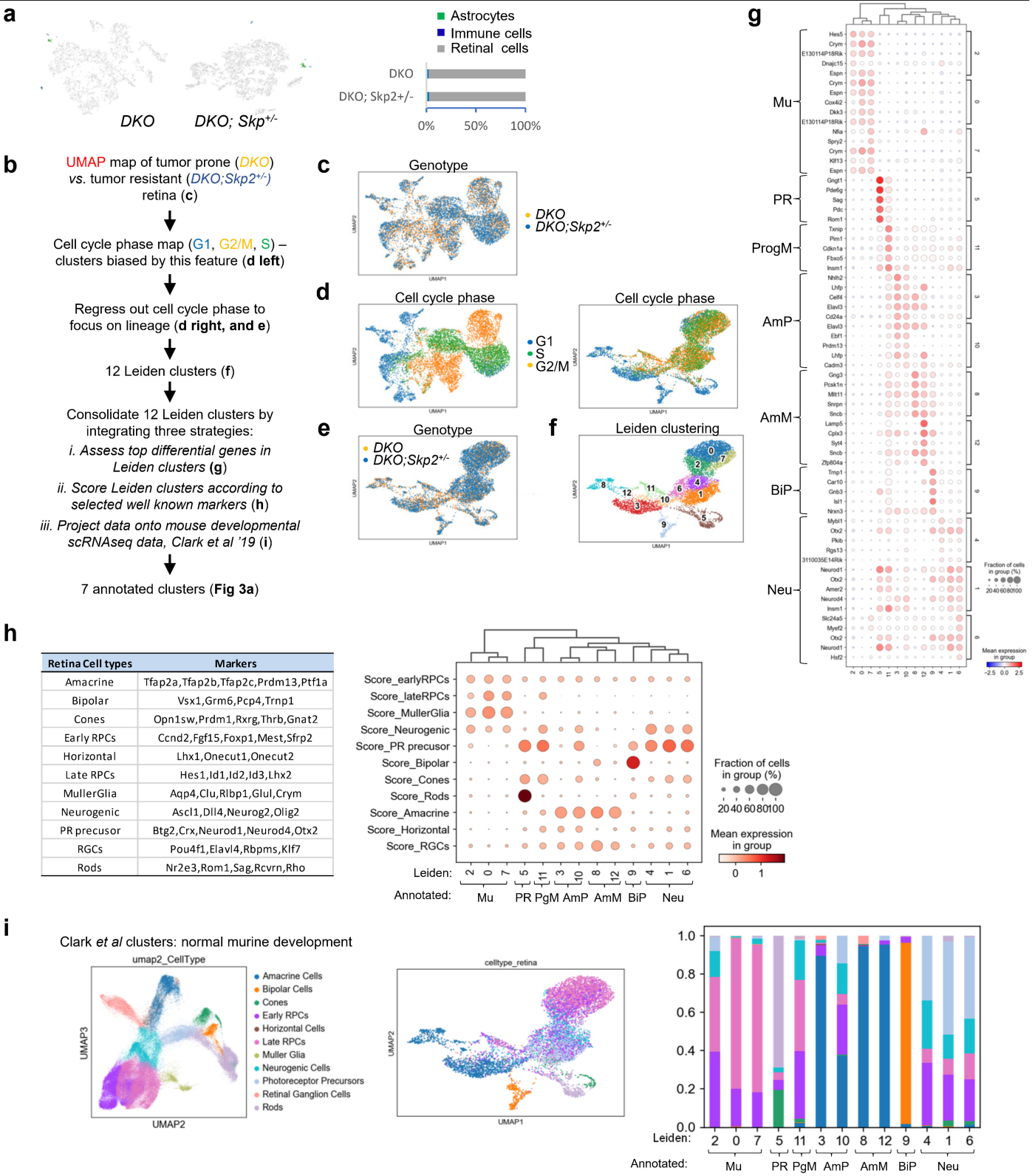

Retina Cell types	Markers
Amacrine	Tfap2a,Tfap2b,Tfap2c,Prdm13,Ptf1a
Bipolar	Vsx1,Grm6,Pcp4,Trnp1
Cones	Opn1sw,Prdm1,Rxrg,Thrb,Gnat2
Early RPCs	Ccnd2,Fgf15,Foxp1,Mest,Sfrp2
Horizontal	Lhx1,Onecut1,Onecut2
Late RPCs	Hes1,Id1,Id2,Id3,Lhx2
MullerGlia	Aqp4,Clu,Rlbp1,Glul,Crym
Neurogenic	Ascl1,Dll4,Neurog2,Olig2
PR precusor	Btg2,Crx,Neurod1,Neurod4,Otx2
RGCs	Pou4f1,Elavl4,Rbpms,Klf7
Rods	Nr2e3,Rom1,Sag,Rcvrn,Rho

Extended Data Fig. 4 | Tumor suppression independent of cell lineage changes. a) UMAP plot (left panel) showing astrocytes (green) and immune cells (blue) based on scRNAseq of P8 *DKO* and *DKO-Skp2*$^{+/-}$ retinas, and quantification (right panel). **b**) The six steps to analyze the scRNAseq data. **c**) The initial clustering UMAP of the scRNAseq data of P8 *DKO* (orange) and *DKO-Skp2*$^{+/-}$ (blue) retinas. **d**) Cells annotated with three cell cycle phases, including G1 (blue), G2/M (orange) and S (green). Left panel: distribution before regressing out cell cycle genes. Right panel: distribution after regressing out cell cycle genes to focus on lineage. **e**) Clustering UMAP of the scRNAseq data of P8 *DKO* (orange) and *DKO-Skp2*$^{+/-}$ (blue) retinas, after regressing out cell cycle genes. **f**) The 12 Leiden clusters in (e). **g**) Dot plot of the top 5 marker genes in each Leiden cluster. Based on this analysis, the 12 Leiden clusters (numbers on the right) were consolidated into 7 clusters (names on the left). **h**) Known marker genes of 11 mouse retinal cell populations (left panel) and dot plot of the scores of each cell population in the scRNAseq data of *DKO* and *DKO-Skp2*$^{+/-}$ retinas (right panel). **i**) Cluster UMAP showing the 11 cell populations during normal murine retinal development (left panel) from Clark et al.[80], and the allocation of these cell types in the UMAP (middle panel) in (f). The graph (right panel) shows the proportion of each cell population in the 12-Leiden clusters.

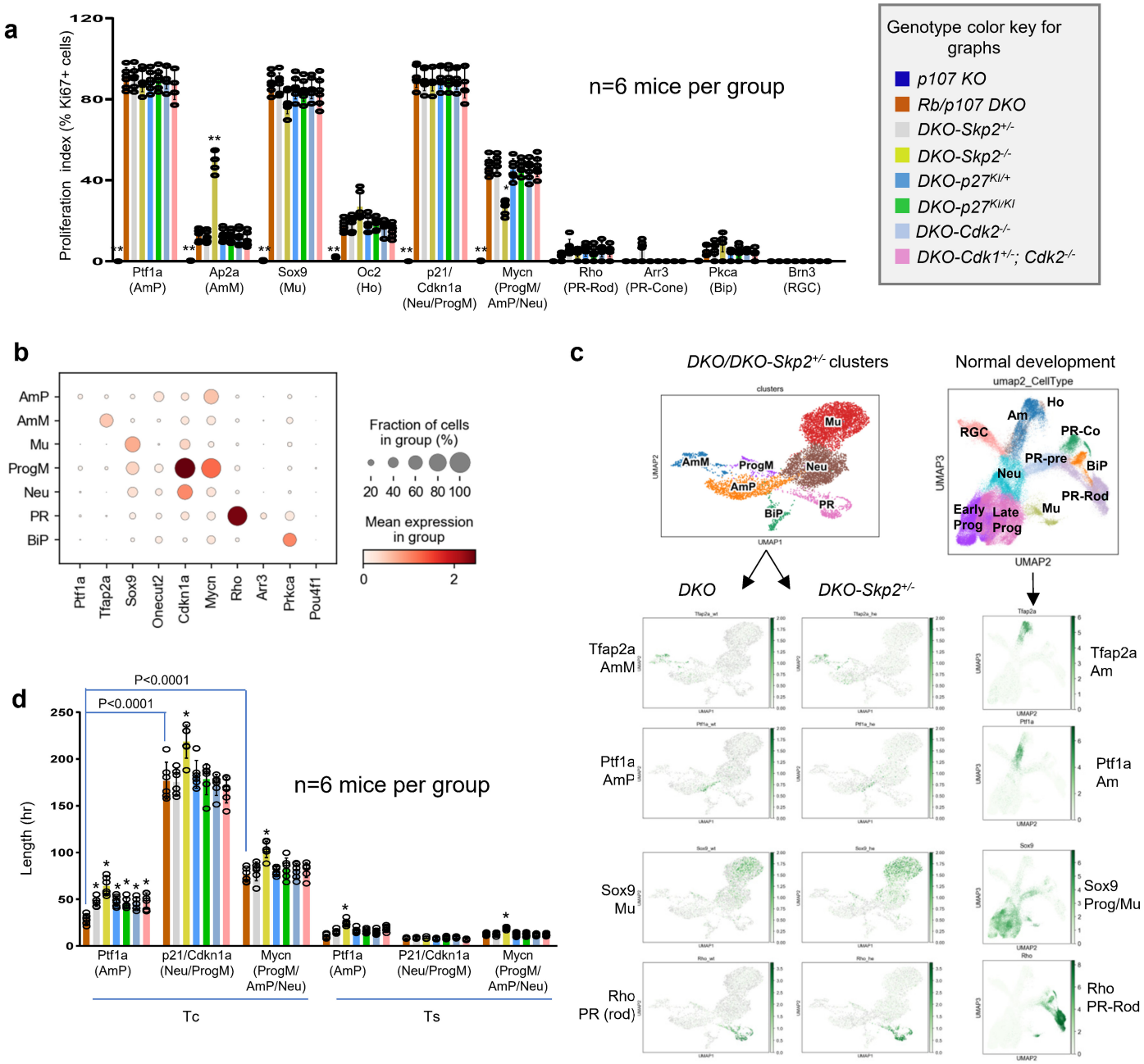

Extended data Fig. 5 | Tracking proliferation index and cell cycle length in multiple clusters. a) Proliferation index (%Ki67$^+$ cells) in the indicated cell types expressing the indicated markers in P8 retinas of indicated genotypes. **b**) Dot plot indicating expression of the markers used in (a) in the seven annotated clusters. **c**) Examples of feature maps for some markers used in (a). The expression of the markers in DKO or DKO-Skp2 +/− retina is shown on the two left panels, while expression in normal development is shown on the right panel. **d**) Tc and Ts of cells expressing the indicated marker proteins.

Data are presented as mean ± s.d. in a and d (n = 6 mice per cohort as indicated by bars). Asterisks: significant difference between *DKO* and the indicated genotypes (*, $p < 0.05$; **; $p < 0.01$, one-way ANOVA, Bonferroni correction). The exact p-values between amacrine precursors (Ptf1a$^+$) and mitotic neural progenitors (p21-Cdkn1a$^+$) or mitotic neural progenitor and amacrine precursors (Mycn$^+$) in *DKO* retinas by two-tailed unpaired t-test are indicated in the figures.

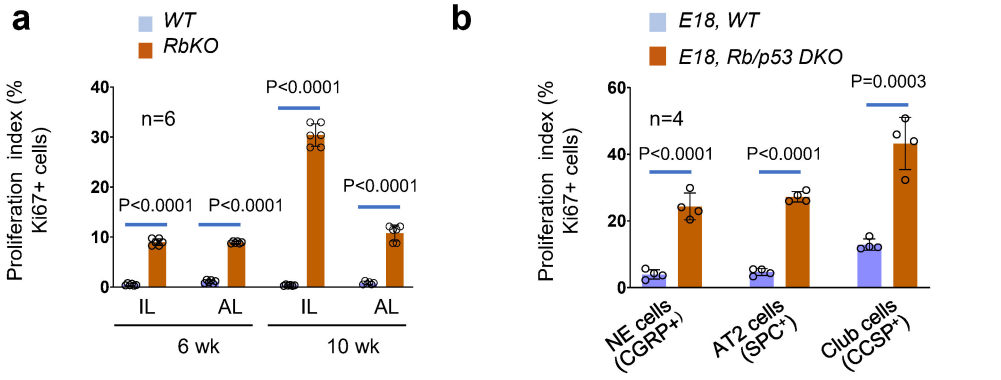

RbKO: 6 wk and 10 wk Pituitary *Rb/p53* DKO: E18 Lung

Extended data Fig. 6 | Proliferation (Ki67) index of *Rb* KO pituitary and *Rb/p53 DKO* E18 lung. a) Proliferation index in the intermediate (IL) and anterior (AL) pituitary lobes of WT (*LSL-tdTomato;Rb$^{f/f}$*) or *Rb* null (*CreERT2; LSL-tdTomato;Rb$^{f/f}$*) mice injected with tamoxifen at 4 or 8 wk and assessed at 6 or 10 wk of age, respectively. **b**) Proliferation index in WT or *Rb/p53 DKO* E18 lung Cgrp^{+} neuroendocrine (NE), Spc^{+} Alveolar type 2 (AT2) and Ccsp^{+} club cells. Data are presented as mean ± s.d. (n = 6 mice for a, n = 4 mice for b per cohort as indicated by bars); The exact p-values between WT/Control *vs.* mutants by two-tailed unpaired t-test are indicated in the figures.

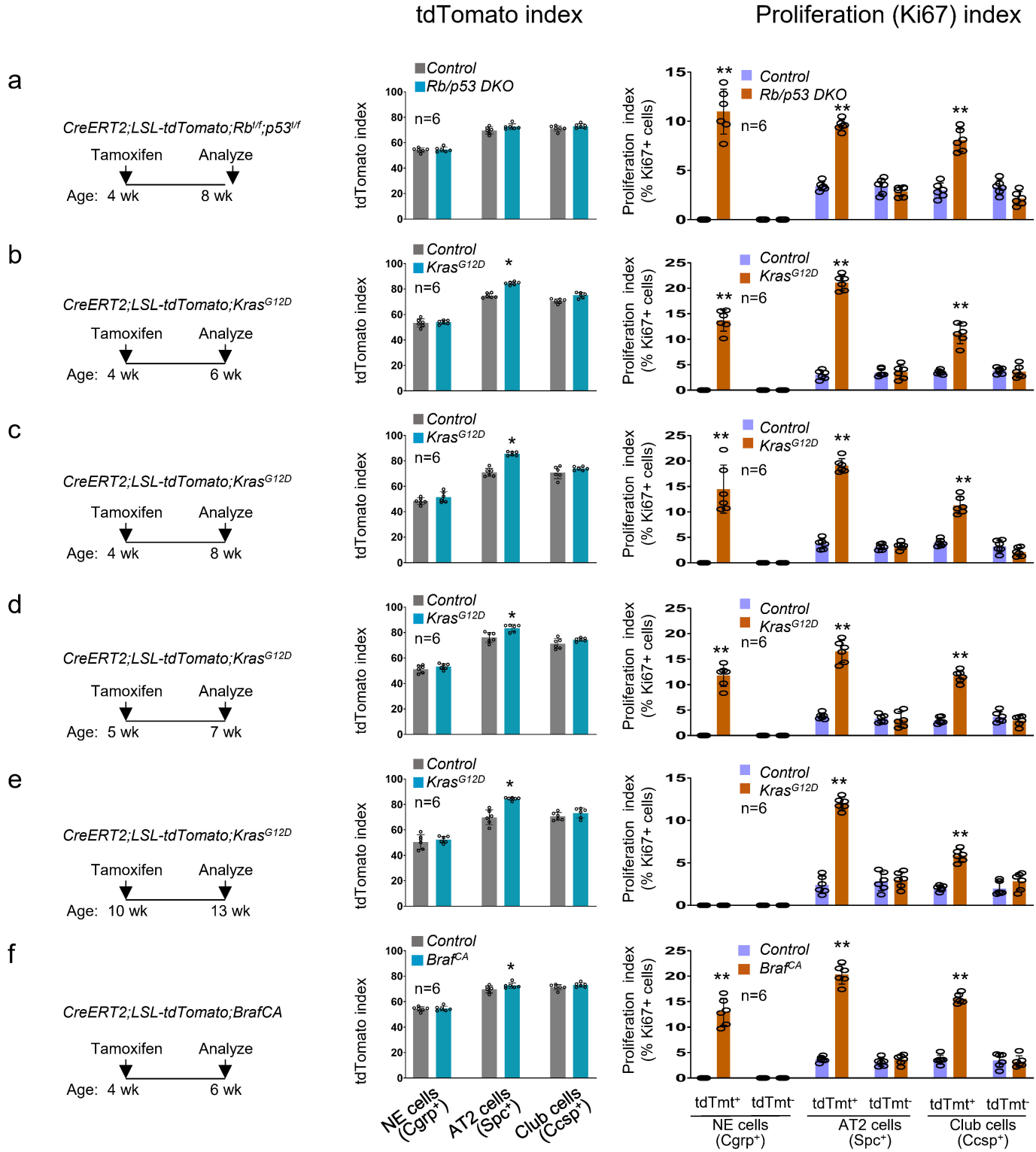

Extended Data Fig. 7 | tdTomato (tdTmt) index and proliferation (Ki67) index of tamoxifen-induced *Rb/p53 DKO*, *Kras^{G12D}* and *BrafCA* mouse lung cells. a) Control (*CreERT2;LSL-tdTomato*) and *Rb/p53 DKO* animals (*CreERT2;LSL-tdTomato;Rb$^{f/f}$;p53$^{f/f}$*) injected with tamoxifen at 4 wk and assessed at 8 wk of age. **b**-**e**) Control (*CreERT2;LSL-tdTomato*) and *Kras* (*CreERT2;LSL-tdTomato;Kras^{G12D}*) mice injected with tamoxifen at: 4 wk and assessed at 6 wk of age (b); 4 wk and assessed at 8 wk of age (c); 5 wk and assessed at 7 wk of age (d); 10 wk and assessed at 13 wk of age (e). **f**) Control (*CreERT2;LSL-tdTomato*) and *BrafCA* animals (*CreERT2;BrafCA;LSL-tdTomato*) injected with tamoxifen at 4 wk and assessed at 6 wk of age. Schematics on the left summarize the experiments. Graphs in the center show tdTmt index of the indicated cell types (grey control, blue oncogenic lesion induced). Graphs on the right show Ki67 index of the indicated cell types for control tdTmt$^+$ or tdTmt$^-$ cells in *CreERT2;LSL-tdTomato* mice or control unrecombined tdTmt$^-$ cells in *CreERT2;LSL-tdTomato; Rb/p53, Kras^{G12D}, or Braf^{CA}* mice (blue bars), or induced tdTmt$^+$ cells in the latter (red bars). Data are presented as mean ± s.d. (n = 6 mice per cohort as indicated by bars); asterisks: significant difference between control *vs.* mutated mice (* $p < 0.05$, ** $p < 0.01$. two-tailed unpaired student's t-test).

nature portfolio

Corresponding author(s): Rod Bremner

Last updated by author(s): March 7, 2025

Reporting Summary

Nature Portfolio wishes to improve the reproducibility of the work that we publish. This form provides structure for consistency and transparency in reporting. For further information on Nature Portfolio policies, see our Editorial Policies and the Editorial Policy Checklist.

Statistics

For all statistical analyses, confirm that the following items are present in the figure legend, table legend, main text, or Methods section.

n/a	Confirmed	
☐	☒	The exact sample size (*n*) for each experimental group/condition, given as a discrete number and unit of measurement
☐	☒	A statement on whether measurements were taken from distinct samples or whether the same sample was measured repeatedly
☐	☒	The statistical test(s) used AND whether they are one- or two-sided *Only common tests should be described solely by name; describe more complex techniques in the Methods section.*
☒	☐	A description of all covariates tested
☐	☒	A description of any assumptions or corrections, such as tests of normality and adjustment for multiple comparisons
☐	☒	A full description of the statistical parameters including central tendency (e.g. means) or other basic estimates (e.g. regression coefficient) AND variation (e.g. standard deviation) or associated estimates of uncertainty (e.g. confidence intervals)
☐	☒	For null hypothesis testing, the test statistic (e.g. *F*, *t*, *r*) with confidence intervals, effect sizes, degrees of freedom and *P* value noted *Give P values as exact values whenever suitable.*
☒	☐	For Bayesian analysis, information on the choice of priors and Markov chain Monte Carlo settings
☒	☐	For hierarchical and complex designs, identification of the appropriate level for tests and full reporting of outcomes
☐	☒	Estimates of effect sizes (e.g. Cohen's *d*, Pearson's *r*), indicating how they were calculated

Our web collection on statistics for biologists contains articles on many of the points above.

Software and code

Policy information about availability of computer code

Data collection	1. Labeled cells were visualized and images were captured using a Nikon Eclipse Ti or Ti2 laser scanning confocal microscope. Measurements were performed with Nikon NIS-Elements AR 3.10 software. 2. Western blots data were collected and analyzed using ODYSSEY Infrared Imaging System (LI-COR). 3. Flow cytometry data were collected on a Gallios flow cytometer and Kaluza analysis software (Beckman Coulter). 4. Single-cell sequencing data were collected using the HiSeq3000 platform (Illumina).
Data analysis	1. Quantitation used Image J (Fuji, version 1.54g). Retinal blood vessels were analyzed by Angiotool (Version 0.6a). 2. Kaplan–Meier survival curves and statistical analysis was performed using the GraphPad Prism software. 3. Western blots data were analyzed using ODYSSEY Infrared Imaging System (LI-COR). 4. Flow cytometry data were analyzed by Kaluza analysis software (Beckman Coulter). 5. Single-cell sequencing data were analyzed by CellRanger pipelines (10x Genomics, V2.2.0), 10x Genomics Loupe Browser, Scanpy python toolkit, Seurat R toolkit, biomaRt package, the python package scrublet

For manuscripts utilizing custom algorithms or software that are central to the research but not yet described in published literature, software must be made available to editors and reviewers. We strongly encourage code deposition in a community repository (e.g. GitHub). See the Nature Portfolio guidelines for submitting code & software for further information.

Data

Policy information about availability of data

All manuscripts must include a data availability statement. This statement should provide the following information, where applicable:

- Accession codes, unique identifiers, or web links for publicly available datasets
- A description of any restrictions on data availability
- For clinical datasets or third party data, please ensure that the statement adheres to our policy

Data files for transcriptomic scRNAseq analyses are available at the Gene Expression Omnibus (GEO) under accession numbers GSE245137. Mouse reference index provided by 10x Genomics (refdata-cellranger-mm10) can be downloaded from: https://www.10xgenomics.com/support/software/cell-ranger-arc/downloads.

Research involving human participants, their data, or biological material

Policy information about studies with human participants or human data. See also policy information about sex, gender (identity/presentation), and sexual orientation and race, ethnicity and racism.

Reporting on sex and gender	*N/A*
Reporting on race, ethnicity, or other socially relevant groupings	*N/A*
Population characteristics	*N/A*
Recruitment	*N/A*
Ethics oversight	*N/A.*

Note that full information on the approval of the study protocol must also be provided in the manuscript.

Field-specific reporting

Please select the one below that is the best fit for your research. If you are not sure, read the appropriate sections before making your selection.

☒ Life sciences ☐ Behavioural & social sciences ☐ Ecological, evolutionary & environmental sciences

For a reference copy of the document with all sections, see nature.com/documents/nr-reporting-summary-flat.pdf

Life sciences study design

All studies must disclose on these points even when the disclosure is negative.

Sample size	Sample size was determined by power analysis (Cohen's d). Different genotypes were compared within the same litter and across four to six litters.
Data exclusions	No data were excluded. Both sex of animals were used in the study.
Replication	Findings were reliably reproduced across four to six litters
Randomization	The experimental approaches did not require samples to be randomized. Samples, and the subsequent data collection and analysis, were handled the same way in all experiments.
Blinding	The investigators were not blinded to group allocation during data collection or subsequent analysis for two reasons: (1) they were performing the experiments themselves and were aware of experimental conditions, groups and outcomes. All mice in each group were analyzed in the same way. (2) Non-blinding also facilitates veterinary and staff monitoring tumor growth.

Reporting for specific materials, systems and methods

We require information from authors about some types of materials, experimental systems and methods used in many studies. Here, indicate whether each material, system or method listed is relevant to your study. If you are not sure if a list item applies to your research, read the appropriate section before selecting a response.

Materials & experimental systems

n/a	Involved in the study
☐	☒ Antibodies
☒	☐ Eukaryotic cell lines
☒	☐ Palaeontology and archaeology
☐	☒ Animals and other organisms
☒	☐ Clinical data
☒	☐ Dual use research of concern
☒	☐ Plants

Methods

n/a	Involved in the study
☒	☐ ChIP-seq
☐	☒ Flow cytometry
☒	☐ MRI-based neuroimaging

Antibodies

Antibodies used

The following antibodies were obtained from commercial sources: Active caspase 3 (Cell Signaling Technology 9661, WB: 1:200, IF:1:500), Ap2a (Santa Cruz SC-8975, IF: 1:500), aPKC zeta (BD Transduction lab 610176, IF: 1:500), BrdU (Abcam ab1893, IF: 1:500;DSHB, G3G4, 1:1000), Brn3 (Santa Cruz SC-6062, IF: 1:500), Calretinin (Santa Cruz SC-11644, IF: 1:500), CCSP (Seven Hills Bioreagent,WRAB-3950, 1:1000), CGRP (Sigma, C8198, 1:1000), Cone arrestin (Millipore AB15282, IF: 1:500), Cyclin A2 (Abcam, Ab181591,1:500),Cyclin B1 (Cell Signaling Technology, 4138S, IF: 1:500), Galectin 3 (Santa Cruz, SC-19283,IF: 1:500), Ki67 (BD science Pharmingen 550609, IF: 1:500; Thermo Fisher Scientific, 14-5698-82,IF:1:500), MSHa (Fisher Scientific,AB508MI, IF:1:200), Mycn(Santa Cruz, SC-791, IF:1:500), N-Cadherin (Santa Cruz SC7939, IF: 1:500), OC2(R&D systems, AB6294, IF: 1:500), P21 cip1 (Abcam,ab188224, IF:1:500), P27 kip1 (BD Biosciences 554069, IF: 1:500, WB: 1:200), Phospho-aPKCzeta/lamda(ThermoFisher 44-968G, IF: 1:500), Phospho-histone H3 (Santa Cruz SC-8656, IF: 1:500),Protein kinase C alpha(Sigma, P5704, IF:1:500), Rhodopsin (Santa Cruz SC-57433, IF: 1:500), Skp2 (SC-74477; Santa Cruz, WB:1:1000), Sox9 (EMD Millipore, MAB5535, IF:1:500), SPC (Abcam, ab40879, 1:1000), beta-actin (A5441, Sigma, WB: 1:2000).Flow cytometry used the following antibodies: anti-B220 (0.5 g, ThermoFisher Scientific Cat# 12-0452-81), anti-CD3 (0.75 g,ThermoFisher Scientific Cat# 17-0032-80), anti-CD335/NKp46 (0.75 g, ThermoFisher Scientific Cat# 12-3351-80), anti-CD45 (0.1 g,ThermoFisher Scientific Cat# 12-0451-82), and anti-CD11b (0.25 g, ThermoFisher Scientific Cat# 17-0112-81). F-actin was labelled by Alexa Fluor® 488 Phalloidin (ThermoFisher Scientific, A12379, IF: 1:500) or Alexa Fluor® 568 Phalloidin(ThermoFisher Scientific, A12380, IF: 1:500). Blood vessel endothelium cells were labelled by FITC-IB4 (Sigma, L2895, 1:200). Crx antibody was from Dr. CY Gregory-Evans at Imperial College School of Medicine. Ptf1a antibody was from Dr. Pierre Cordelier,INSERM, France.

Validation

The vendors validated the commercially available antibodies, Phalloidin and IB4.
Crx antibody had been validated by Dr. CY Gregory-Evans: Bibb LC et al., Temporal and spatial expression patterns of the CRX transcription factor and its downstream targets. Critical differences during human and mouse eye development. Human Molecular Genetics, 2001, 10 (15): 1571-1579; in our previous studies, see Chen D, Livne-bar I, Vanderluit JL, Slack RS, Agochiya M, Bremner R. Cell-specific effects of RB or RB/p107 loss on retinal development implicate an intrinsically death-resistant cell-of-origin in retinoblastoma. Cancer Cell. 2004 Jun;5(6):539-51.
Ptf1a antibody had been validated by Dr. Pierre Cordelier: Hanoun et al., The E3 ubiquitin ligase thyroid hormone receptor-interacting protein 12 targets pancreas transcription factor 1a for proteasomal degradation J Biol Chem. 2014 Dec 19;289(51):35593-604.

Animals and other research organisms

Policy information about studies involving animals; ARRIVE guidelines recommended for reporting animal research, and Sex and Gender in Research

Laboratory animals

α-Cre mice (P. Gruss, age E14-P400), B6.129P2(Cg)-Braftm1Mmcm/J (Jackson Laboratory, strain# 017837, Common Name: BRafCA, age P0-P42), B6.Cg-Gt (ROSA)26Sortm14(CAG-tdTomato)Hze/J, also known as Ai14(tdTomato) (Jackson Laboratory, stock#007914, age P0-P91), B6.129-Gt (ROSA)26Sortm1(cre/ERT2) Tyj/J (Jackson Laboratory, Stock No: 008463, age P0-P91), B6.129S4-Krastm4Tyj/J (Jackson Laboratory, Stock No: 008179, age P0-P91), Cdk1f/f (D.Santamaria and M. Barbacid, age P0-P400), Cdk2f/f (D. Santamaria and M. Barbacid, age P0-P400) , p107-/- mice (M.Rudnicki, age E14-P400), p27Ck-/Ck- mice (A. Besson and Roberts, age P0-P400), p27T187A (A. Besson and J. Roberts, age P0-P400), P53f/f mice (A. Berns, age E18-P56), Rbf/f mice (A.Berns, age E14-P400), Skp2-/- mice (K. Nakayama, age P0-P400), Spc-rtTA(Whitsett, age E18-P60), TetO-Cre (Whitsett, age E18-P60) and Z/Red (Jackson Laboratory, stock#005438, age E16) mice

Wild animals

Study did not involve wild animals

Reporting on sex

No studies have reported sex-dependent differences in the tumor types examined, thus sex was not assessed.

Field-collected samples

The study did not involved field samples.

Ethics oversight	Mice were treated according to institutional and national guidelines approved by the Toronto Centre for Phenogenomics and Cincinnati Children's Hospital Medical Center.

Note that full information on the approval of the study protocol must also be provided in the manuscript.

Flow Cytometry

Plots

Confirm that:

☒ The axis labels state the marker and fluorochrome used (e.g. CD4-FITC).

☒ The axis scales are clearly visible. Include numbers along axes only for bottom left plot of group (a 'group' is an analysis of identical markers).

☒ All plots are contour plots with outliers or pseudocolor plots.

☒ A numerical value for number of cells or percentage (with statistics) is provided.

Methodology

Sample preparation	1. P8 eyeballs of p107-/-, α-Cre; Rbf/f;p107-/- and α-Cre; Rbf/f;p107-/-; Skp2+/- mice were enucleated, and peripheral retinas were dissected in fresh cold 1X HBSS. 2. Dissected peripheral retinas were transferred to 200µl of cold HBSS per retina. 3. An equivalent amount of Papain solution was added and incubated at 37°C for 10 min, and the tube inverted gently every 2 min. 4. Next, the digestion solution was discarded by pipetting without disturbing the retina. 5. Mechanical trituration of the retina was performed in 600µl of Neurobasal Media supplemented with 10% FBS by pipetting slowly 10 to 15 times with a P1000 pipette tip. 6. Samples were then DNAse treated for 5 min at 37°C. 7. Cell suspensions were centrifuged using a swing-bucket rotor at 200×g for 5 min. 8. The supernatant was carefully aspirated off the cell pellet, and the pellet was suspended in 1-5ml Neurobasal media with 1% FBS. 9. Cellular aggregates were removed by straining cells through a 50 µm cell strainer (pluriSelect). 10. Splenocytes were collected by grinding a p107-/- mouse spleen through a 40µm mesh and then red blood cells (RBC) were removed by incubating cells for 10 min in RBC lysis buffer (Sigma, Cat# 11814389001).
Instrument	Gallios flow cytometer
Software	Kaluza analysis software (Beckman Coulter)
Cell population abundance	FACS analysis of dissociated tumor-prone DKO and tumor-resistant DKO-Skp2+/- retina revealed very low levels of B, T, or NK cells, macrophage/microglia, or leukocytes in both genotypes
Gating strategy	Cells were first gated on Forward Scatter by Side Scatter Density Plots to exclude debris. The resulting cells (~90% of total) then underwent doublet exclusion by comparing Forward Scatter Peak Height vs. Forward Scatter Time-of-flight (or peak width) and then again for Side Scatter Peak Height vs. Side Scatter Time-of-flight. Approximately 0.5% of the cells were excluded as doublets at this stage. Finally, the triple-gated cells (FS x SS, 2 rounds of doublet exclusion) were analyzed using Single Parameter Histograms to identifying cells positive for each marker. Isotype control antibodies were used to define negative cells and splenocytes were used as a positive control to define positive cells.

☒ Tick this box to confirm that a figure exemplifying the gating strategy is provided in the Supplementary Information.